

Investigating the normal and tangential peeling behaviour of gecko spatulae using a coupled adhesion-friction model

Saipraneeth Gouravaraju¹, Roger A. Sauer², and Sachin Singh Gautam^{*1}

¹Indian Institute of Technology Guwahati, Guwahati, India 781039

²Aachen Institute for Advanced Study in Computational Engineering Science (AICES), RWTH Aachen University, Templergraben 55, 52056 Aachen, Germany

Abstract

The present work investigates the normal and tangential peeling behaviour of a gecko spatula using a coupled adhesion-friction model. The objective is to explain the strong attachment and easy detachment behaviour of the spatulae as well as to understand the principles behind their optimum design. Using nonlinear finite element computations, it is shown that during *tangentially-constrained* peeling the partial sliding of the spatula pad near the peeling front stretches the spatula, thus increasing the strain energy and leading to high pull-off forces. The model is used to investigate the influence of various parameters on the pull-off forces – such as the peeling angle, spatula shaft angle, strip thickness, and material stiffness. The model shows that increasing the spatula pad thickness beyond a certain level does not lead to a significant increase in the attachment forces. Further, the easy detachment behaviour of geckos is studied under *tangentially-free* peeling conditions. It is found that the spatulae readily detach from the substrate by changing their shaft angle and eventually peel vertically like a tape. Since the present computational model is not limited by the geometrical, kinematical, and material restrictions of theoretical models, it can be employed to analyse similar biological adhesive systems.

Keywords: Contact mechanics, nonlinear finite element analysis, van der Waals adhesion, dry friction, gecko adhesion, peeling

1 Introduction

The underside of each digit on the gecko toes is covered by hundreds of thousands of micro-fibrils called setae, which further branch into hundreds of nanoscale spatula-like structures [1, 2, 3]. These spatulae adhere to the substrate using intermolecular van der Waals forces [4, 5, 6]. In their pioneering work, Autumn et al. [5] measured that a single seta of a Tokay Gecko, with proper orientation, perpendicular preloading, and a parallel drag on the substrate, generates frictional forces as high as approximately 200 μN .

In the last two decades, researchers have extensively studied the structure, function, properties, and applications of the gecko adhesive system [7, 8, 9, 10, 11, 12, 13]. Sitti and Fearing [14] modeled

*Corresponding Author, email: ssg@iitg.ac.in

the spatulae as cantilever beams to study the effect of length, diameter, stiffness, and density. Gao et al. [15] used finite elements with cohesive zone models to analyse the adhesion of a gecko seta. They observed that the seta detaches when the angle between the applied tensile load and the substrate becomes more than 30° . Huber et al. [16] used atomic force microscopy to measure the adhesive forces for a single seta with only four spatulae. Their load-drag-pull experiments revealed that when the spatulae are pulled vertically the maximum pull-off force for a single spatula is close to 10 nN.

Tian et al. [17] proposed a theoretical model for estimating the adhesion and friction forces between a single spatula and a rigid substrate. However, they did not consider how the frictional forces vary within the peel zone. They also did not consider the elastic loading and unloading of the spatula as it is being pulled. Pesika et al. [18] proposed a peel-zone model similar to Kendall's peeling model [19] but differing in an angle-dependent multiplier. Chen et al. [20] used the Kendall peeling model and finite element analysis to study the effect of pre-tension on the spatula peeling characteristics such as peeling force, peeling angle, and critical detachment angle. Begley et al. [21] presented an analytical mode that accounts for the frictional sliding of single and double sided peeling of an elastic tape. They found that the critical force required for peeling is higher for the case of frictional sliding than for pure sticking. Peng and Chen [22] used an analytical model derived from the principle of minimum potential energy to examine the effect of bending stiffness on the peeling force. Labonte and Federle [23] studied the coupling of adhesion and friction in insects and showed that there is a linear relationship between friction and adhesion for large friction forces. The authors proposed that the large peeling forces at small peeling angles could be due to pre-tension arising from partial sliding close to the peeling front during detachment of the adhesive pads. Kim and Varenberg [24] studied how the pulling angle influences the normal and tangential components of the pull-off force for wall-shaped adhesive microstructures using Kendall's peeling model [19]. Peng et al. [25] studied the peeling behaviour of finite length thin-films using both theoretical and finite element models. They observed that unlike classical peeling models like Kendall's, which consider infinite film length, finite film length models lead to steady-state peeling process depending on the initial adhesion length. A detailed review of many adhesion and friction models of geckos along with advancements in gecko inspired synthetic adhesives can be found in the review papers by Kwak and Kim [26], Jagota and Hui [27], Zhou et al. [28], Kasar et al. [29], Seale et al. [30], Russell et al. [31], and Labonte and Federle [32].

Analytical models, based on simplified seta/spatula geometries combined with linear deformation behaviour offer limited insight into the details of seta and spatula adhesion, deformation, and stresses [33]. Therefore, Sauer [34, 35] presented a nonlinear multi-scale frame work for studying seta and spatula adhesion based on the coarse-graining of van der Waals interaction [36]. The multi-scale model was improved by Sauer and Holl [37], by accounting for the detailed 3-D spatula geometry. Using a geometrically exact finite beam model [42], Sauer [38] studied the effect of bending stiffness on spatula adhesion. Peng et al. [39] employed a cohesive zone model to study the influence of different parameters on the peeling behaviour of a spatula. Cheng et al. [40] examined how a non-uniform pre-tension is generated when the spatula slides on the substrate during attachment. Gautam and Sauer [41] analysed gecko adhesion using a dynamic FE model. Using the geometrically exact beam formulation of [42], Mergel et al. [43] showed that the optimal shape of a peeling strip is similar to that of a gecko spatula. Mergel and Sauer [44] extended the study to incorporate tangential contact. A detailed review of different computational methods used for solving adhesive contact is presented in [45].

The frictional behaviour of gecko setae is unlike other materials. When the setae are dragged

proximally (towards the animal) along their natural curvature it results in tensile loading of the seta and yet under these tensile loads they display strong static and kinematic friction that disagrees with the Amontons’ law [46]. In many of the analytical and computational models of gecko adhesion, the effect of friction is neglected. But it is known from experiments [5] that at small angles, the large adhesion forces that the gecko generates are determined mainly by frictional forces. Friction in general, emerges from different mechanisms at the molecular level. Major mechanisms that contribute to friction are: interlocking, wear, plastic deformation, adhesion, asperity deformation, viscous dissipation, and fracture [47]. Therefore, a number of studies attempted to model friction due to adhesion. In the current work, the focus is on coupling of adhesion and friction, which is a major factor in gecko adhesion [46].

Derjaguin [48] generalized Amontons’ law of friction to include an additional parameter to account for adhesion. Majidi et al. [49] proposed a friction model based on this generalized Amontons’ law for microfiber arrays. In their description, the frictional force is related to the normal load, through an effective friction coefficient μ_{eff} that is a function of the sliding friction coefficient between the bodies and the interfacial shear strength per unit area τ . Gravish et al. [50] studied the effect of sliding velocity on setal adhesion. They found that the setae became more sticky with increasing velocity. Puthoff et al. [51] studied the effect of material properties and atmospheric humidity on dynamic friction characteristics of natural and synthetic gecko setal arrays. Classical van der Waals interaction can be described by the Lennard-Jones potential and this does not contain any frictional contribution. Jiang and Park [52] used an additional “frictional potential” to describe the friction properties of layered materials. Many researchers have used cohesive zone models [55, 53, 54] with friction according to Coulomb’s law to analyze sliding friction. Recently, Mergel et al. [56] have developed two new continuum contact models for friction due to adhesion that can capture sliding friction even under tensile loads. The first model, “Model DI”, assumes that the sliding traction during adhesion is independent of the normal distance and is equal to a constant frictional shear strength, which is related to the maximum adhesive traction. In their second model, “Model EA”, the sliding traction varies with the normal distance and is dependent on the normal traction.

From the literature presented, which is by no means is an exhaustive list, it is clear that there are considerable efforts dedicated to modeling, understanding, and explaining coupled adhesion and friction in geckos. However, existing models have many shortcomings due to the intrinsic complexity of the gecko’s hierarchical adhesion system. One of the aspects of gecko adhesion that has not yet been fully explored is the coupling of adhesion and friction at the spatula level. As such, the present work aims to model and understand coupled adhesion and friction in gecko spatula peeling. The peeling behaviour of a gecko spatula is studied here through a computational model. To the best of our knowledge, there has been no earlier detailed computational study in the literature that explores the coupling of adhesion and friction in gecko adhesion. For the present study, a combination of the adhesion model of Sauer and Li [36] and the friction model “Model EA” proposed by Mergel et al. [56] is used. A two-dimensional strip is considered to represent the gecko spatula as done by many other researchers [17, 20, 39]. The peeling of the strip is simulated within a nonlinear finite element framework.

2 Mathematical Formulation

In this section, the computational formulation for adhesive frictional contact between the spatula and a flat rigid substrate is presented. The coarse grained contact model (CGCM) of [36] is used.

The contribution of tangential friction due to normal adhesion forces is derived from one of the coupled adhesion and friction models viz. “Model EA” of [56].

2.1 Weak Form

The weak form governing the interaction of the deformable spatula with the rigid substrate can be written as

$$\int_{\Omega} \text{grad}(\delta\boldsymbol{\varphi}) : \boldsymbol{\sigma} \, dv - \int_{\partial_c\Omega} \delta\boldsymbol{\varphi} \cdot \mathbf{t}_c \, da - \delta\Pi_{\text{ext}} = 0, \quad \forall \delta\boldsymbol{\varphi} \in \mathcal{V}, \quad (1)$$

where \mathcal{V} represents the space of kinematically admissible variations of deformation field $\boldsymbol{\varphi}$, and $\delta\Pi_{\text{ext}}$ denotes the virtual work of the external forces acting on the spatula. $\boldsymbol{\varphi}$ is defined as the motion mapping any arbitrary point \mathbf{X} in the reference configuration Ω_0 of the spatula to the deformed current location $\mathbf{x} \in \Omega$ and is given by $\mathbf{x} = \boldsymbol{\varphi}(\mathbf{X})$.

The first term in Eq. (1) represents the internal virtual work of the Cauchy stress tensor $\boldsymbol{\sigma}$. For elastic material behaviour, this can be obtained from the variation of the internal energy Π_{int} [37]

$$\Pi_{\text{int}} = \int_{\Omega_0} W(\mathbf{F}) \, dV. \quad (2)$$

In this study, a nonlinear Neo-Hookean material is considered, for which the strain energy density function W is given by

$$W(\mathbf{F}) = \frac{\Lambda}{2} (\ln J)^2 + \frac{\mu}{2} (\text{tr}(\mathbf{F}\mathbf{F}^T) - 3) - \mu \ln J, \quad (3)$$

where $\mathbf{F} = \text{Grad}(\boldsymbol{\varphi})$ denotes the deformation gradient and $J = \det(\mathbf{F})$ the volume change. Λ and μ are the Lamé constants and are given as [57]

$$\mu = \frac{E}{2(1+\nu)}, \quad \Lambda = \frac{2\mu\nu}{(1-2\nu)}. \quad (4)$$

The contact traction \mathbf{t}_c in the second term of Eq. (1) is equal to the sum of the tractions due to adhesion, \mathbf{t}_a , and friction, \mathbf{t}_f , i.e.

$$\mathbf{t}_c = \mathbf{t}_a + \mathbf{t}_f. \quad (5)$$

Sauer and Li [36] defined the following two material parameters that govern weak form (1),

$$\gamma_W = \frac{E}{\left(\frac{A_H}{2\pi^2 r_0^3}\right)}, \quad \gamma_L = \frac{R_0}{r_0}, \quad (6)$$

where E and R_0 represent an energy density (or stiffness) and a global length scale chosen for the system, respectively. Here, A_H denotes Hamaker’s constant, and r_0 is the equilibrium distance of the original Lennard-Jones potential [58]

$$\phi(r_d) := \epsilon \left[\left(\frac{r_0}{r_d}\right)^{12} - 2 \left(\frac{r_0}{r_d}\right)^6 \right], \quad (7)$$

where ϵ is an energy scale and r_d is the distance between two points in the interacting bodies.

The second parameter in Eq. (6), γ_L , is the ratio of the global length scale R_0 used to normalize the geometry and the local length scale r_0 . From the definitions, it can be seen that, γ_W characterises the material stiffness in relation to the strength of adhesion, whereas γ_L characterises the overall size of the geometry with respect to the range of adhesion.

It should be noted that γ_W and γ_L are related to the dimensionless Tabor parameter [59]

$$\mu_{\text{Tabor}} = \left(\frac{\sqrt[3]{15} \pi}{8} \right)^{2/3} \left(\frac{\gamma_L}{(\gamma_W)^2} \right)^{1/3}. \quad (8)$$

2.2 Adhesive and Frictional Traction

The adhesive contact traction \mathbf{t}_a is obtained from the variation of the adhesive contact potential as [33]

$$\mathbf{t}_a = t_a \mathbf{n}_p, \quad t_a = \frac{A_H}{2\pi r_0^3 J_1 J_2} \left[\frac{f_1}{45} \left(\frac{r_0}{r_s} \right)^9 - \frac{f_2}{3} \left(\frac{r_0}{r_s} \right)^3 \right], \quad (9)$$

where f_1 and f_2 are curvature dependent parameters of the interacting surfaces and r_s denotes the distance between the spatula and the substrate. Further, J_1 and J_2 represent the volume change of the spatula and the substrate at the surface, respectively. In the current work, as the substrate is considered rigid, $J_2 = 1$. Further, \mathbf{n}_p denotes the surface orientation of the substrate and is constant for flat surfaces. The adhesive traction can also be written with respect to the reference configuration, giving

$$\mathbf{T}_a = T_a \mathbf{n}_p, \quad T_a = \frac{A_H}{2\pi r_0^3 J_2} \left[\frac{f_1}{45} \left(\frac{r_0}{r_s} \right)^9 - \frac{f_2}{3} \left(\frac{r_0}{r_s} \right)^3 \right]. \quad (10)$$

To avoid ill-conditioning, the adhesive traction is regularised for very small normal gaps $r_s \rightarrow 0$. This is done by the linear extrapolation [56]

$$T_a(r_s) = \begin{cases} T_a(r_s), & r_s \geq r_{\text{reg}}, \\ T_a(r_{\text{reg}}) + T'_a(r_{\text{reg}})(r_s - r_{\text{reg}}), & r_s < r_{\text{reg}}, \end{cases} \quad (11)$$

where r_{reg} is a regularisation distance and is chosen to be equal to equilibrium distance r_{eq} [56]. T'_a indicates the derivative of the adhesive traction T_a with respect to r_s and is given as

$$T'_a(r_s) = \frac{\partial T_a(r_s)}{\partial r_s} = -\frac{A_H}{2\pi r_0^4} \left[\frac{1}{5} \left(\frac{r_0}{r_s} \right)^{10} - \left(\frac{r_0}{r_s} \right)^3 \right]. \quad (12)$$

To obtain the contribution of friction due to normal adhesive forces, ‘‘Model EA’’ of [56], is used. If the magnitude of the tangential traction $T_f = \|\mathbf{T}_f\|$ exceeds a certain sliding threshold T_{slide} , the surfaces no longer stick together and start sliding. Before defining the sliding threshold, a cut-off distance r_{cut} , which is the distance up to which the frictional forces are active between the interacting surfaces, is defined as

$$r_{\text{cut}} = s_{\text{cut}} r_{\text{max}} + (1 - s_{\text{cut}}) r_{\text{eq}}, \quad s_{\text{cut}} \in [0, 1], \quad (13)$$

where r_{\max} is the distance at which the adhesive traction T_a given by Eq. (10) reaches the global minimum (maximum attraction) and r_{eq} is the equilibrium distance where the adhesive traction becomes zero, see Figure 1. Then, the sliding threshold is defined as (see Figure 1),

$$T_{\text{slide}}(r_s) = \begin{cases} \frac{\mu_s}{J_{\text{cl}}} [T_a(r_s) - T_a(r_{\text{cut}})], & r_s < r_{\text{cut}}, \\ 0, & r_s \geq r_{\text{cut}}, \end{cases} \quad (14)$$

where J_{cl} is the local surface stretch of the neighbouring body ($= 1$ if the neighbouring body is rigid). For biological adhesives, the static friction coefficient takes similar values as the kinetic friction coefficient [56]. As such, in this work, it is assumed that the value of the friction coefficient μ_s is the same for sticking and sliding.

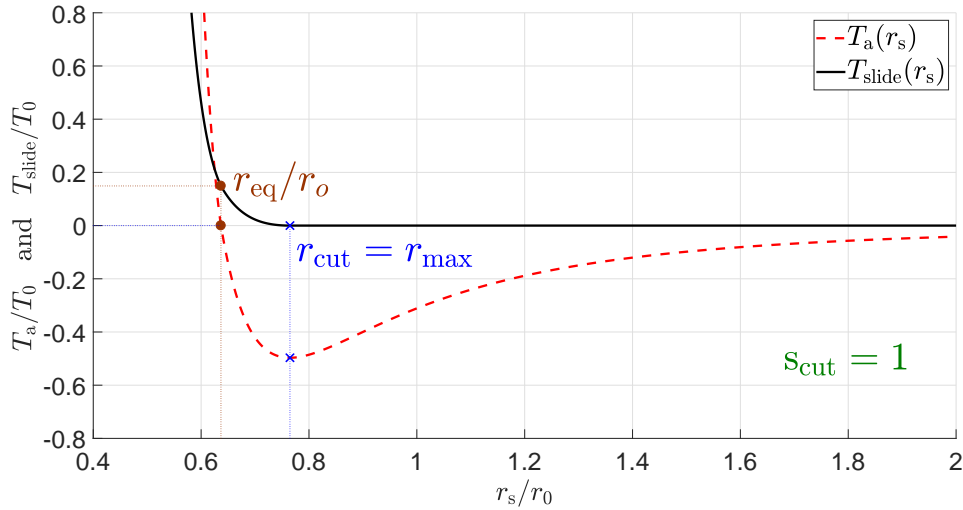


Figure 1: Variation of adhesive traction T_a and sliding threshold T_{slide} with the normal distance r_s according to adhesive friction model “EA” of Mergel et al. [56]. Here, $T_0 = A_H/(2\pi r_0^3)$, $\mu_s = 0.3$, and $s_{\text{cut}} = 1$.

Then, the tangential contact traction $\mathbf{T}_f(\mathbf{r}_s, \mathbf{r}_T)$ is a function of both normal gap \mathbf{r}_s and tangential slip \mathbf{r}_T and depending on whether the bodies are sticking or slipping, it satisfies the following condition

$$\|\mathbf{T}_f(\mathbf{r}_s, \mathbf{r}_T)\| \begin{cases} = T_{\text{slide}} & \text{for sliding,} \\ < T_{\text{slide}} & \text{for sticking.} \end{cases} \quad (15)$$

Frictional laws are often formulated in analogy to constitutive equations describing elasto-plasticity in continuum mechanics [60]. Therefore, the tangential gap is assumed to consist of a sticking part \mathbf{r}_T^e , corresponding to the elastic deformation and a sliding part \mathbf{r}_T^s , corresponding to inelastic or plastic deformation, i.e.,

$$\mathbf{r}_T = \mathbf{r}_T^e + \mathbf{r}_T^s. \quad (16)$$

A linear force-gap dependence during sticking is used to calculate the tangential traction, which corresponds to a penalty regularisation of the sticking constraint as

$$\mathbf{T}_f = -\varepsilon_T \mathbf{r}_T^e, \quad (17)$$

where the ε_T is equivalent to the elasticity modulus. To determine the gap \mathbf{r}_T^s due to sliding, an evolution equation is required, which is derived from the principle of maximum dissipation. The dissipation due to the plastic slip \mathbf{r}_T^s and the relative plastic tangential velocity $\dot{\mathbf{r}}_T^s$ is given as

$$\mathcal{D}_s = -\mathbf{T}_f \cdot \dot{\mathbf{r}}_T^s \geq 0. \quad (18)$$

Next, consider a domain of feasible contact tractions

$$\mathbb{E}_t := \{\mathbf{T}_f \in \mathbb{R}^2 \mid f_s(\mathbf{T}_f) \leq 0\}, \quad (19)$$

where the set f_s contains all the possible tangential tractions \mathbf{T}_f^* that satisfy,

$$f_s = \|\mathbf{T}_f^*\| - \|\mathbf{T}_{\text{slide}}\| \leq 0. \quad (20)$$

According to the principle of maximum dissipation: for the given inelastic/plastic slip velocity $\dot{\mathbf{r}}_T^s$, the true tangential traction \mathbf{T}_f resisting the sliding motion is such that it maximizes the dissipation \mathcal{D}_s [60] i.e.,

$$(\mathbf{T}_f - \mathbf{T}_f^*) \cdot \dot{\mathbf{r}}_T^s \geq 0 \quad \forall \mathbf{T}_f^* \in \mathbb{E}_t, \quad (21)$$

which leads to the constitutive evolution equation for the plastic slip,

$$\dot{\mathbf{r}}_T^s = \gamma \mathbf{n}_T \quad \text{with} \quad \mathbf{n}_T = \frac{\mathbf{T}_f}{\|\mathbf{T}_f\|}, \quad (22)$$

where the parameter $\gamma \geq 0$ is computed from the Karush-Kuhn-Tucker conditions of plasticity given by

$$\gamma \geq 0, \quad f_s(\mathbf{T}_f) \leq 0, \quad \gamma \cdot f_s(\mathbf{T}_f) = 0. \quad (23)$$

For solving Eq. (20) and Eq. (22), a predictor-corrector algorithm is used, see Algorithm 1. The approach is similar to classic friction algorithms [60].

Algorithm 1: Predictor-Corrector algorithm for adhesive friction with rigid substrates.

1. Known values at pseudo-time $t, t + \Delta t$: $\mathbf{r}_T^t, \mathbf{r}_T^{t+\Delta t}, (\mathbf{T}_a)^{t+\Delta t}$
2. Compute trial step (Predictor):

$$(\mathbf{T}_f)_{\text{tr}}^{t+\Delta t} = -\varepsilon_T [(\mathbf{r}_T)^{t+\Delta t} - (\mathbf{r}_T^s)^t]$$

$$(f_s)_{\text{tr}}^{t+\Delta t} = \|(\mathbf{T}_f)_{\text{tr}}^{t+\Delta t}\| - \|(\mathbf{T}_{\text{slide}})^{t+\Delta t}\|$$
3. Check: **if** $(f_s)_{\text{tr}}^{t+\Delta t} \leq 0$ **then**

$$\text{sticking; set } \Delta\gamma^{t+\Delta t} = \frac{\|(\mathbf{T}_f)_{\text{tr}}^{t+\Delta t}\| - \|(\mathbf{T}_{\text{slide}})^{t+\Delta t}\|}{-\varepsilon_T} = 0;$$

go to step 5.

elseif $(f_s)_{\text{tr}}^{t+\Delta t} > 0$ **then**

sliding ; go to step 4.
4. Radial return mapping (Corrector):

Solve $(f_s)_{\text{tr}}^{t+\Delta t} = 0$ for $\Delta\gamma^{t+\Delta t}$

go to step 5.

$$\Delta\gamma^{t+\Delta t} = \frac{\|(\mathbf{T}_f)_{\text{tr}}^{t+\Delta t}\| - \|(\mathbf{T}_{\text{slide}})^{t+\Delta t}\|}{-\varepsilon_{\text{T}}}$$

5. Update: $(\mathbf{T}_f)^{t+\Delta t} = (\mathbf{T}_f)_{\text{tr}}^{t+\Delta t} - \Delta\gamma^{t+\Delta t} \epsilon_{\text{T}} \mathbf{n}_{\text{T}}^{t+\Delta t}$

where $\mathbf{n}_{\text{T}}^{t+\Delta t} = \frac{(\mathbf{T}_f)_{\text{tr}}^{t+\Delta t}}{\|(\mathbf{T}_f)_{\text{tr}}^{t+\Delta t}\|}$

$$(\mathbf{r}_{\text{T}}^s)^{t+\Delta t} = (\mathbf{r}_{\text{T}}^s)^t + \Delta\gamma^{t+\Delta t} \mathbf{n}_{\text{T}}^{t+\Delta t}$$

go to step 1.

3 Finite Element Formulation

Next, the finite element (FE) formulation used for the coupled adhesion-friction model, which is employed to analyse the peeling of a gecko spatula from a flat rigid substrate, is presented. Further, the surface enrichment strategy used in the FE discretization is also discussed. It should be noted that this is a deterministic formulation.

3.1 FE discretization of the weak form

The weak form in Eq. (1) is discretized using the finite element method. Therefore, the spatula is discretized into a number of volume and surface elements containing n_e nodes ($= n_{ve}$ for a volume element and n_{se} for a surface element, respectively). In each element, the displacement field \mathbf{u} and its variation φ is then approximated by the interpolations

$$\mathbf{u}(\mathbf{x}) \approx \mathbf{N}_e(\mathbf{x})\mathbf{u}^e, \quad \delta\varphi(\mathbf{x}) \approx \mathbf{N}_e(\mathbf{x})\mathbf{v}^e, \quad (24)$$

where \mathbf{u}^e and \mathbf{v}^e are the nodal displacement and variations of element e , and the matrix \mathbf{N}_e is a matrix formed by n_e shape functions of the element and is given by

$$\mathbf{N}_e = [N_1^e \mathbf{I}, \quad N_2^e \mathbf{I}, \quad \dots \quad N_{n_e}^e \mathbf{I}], \quad (25)$$

where \mathbf{I} represents the identity tensor.

Using the relations in Eq. (24) and performing an assembly over all the volume and surface elements, the weak form in Eq. (1) can then be rewritten into

$$\mathbf{v}^T [\mathbf{f}_{\text{int}} + \mathbf{f}_{\text{c}} - \mathbf{f}_{\text{ext}}] = \mathbf{0}, \quad \forall \mathbf{v} \in \mathcal{V}_k, \quad (26)$$

where \mathbf{f}_{int} , \mathbf{f}_{c} , and \mathbf{f}_{ext} denote the global internal, contact, and external nodal force vectors, respectively. In the current work, as there are no external forces acting on the spatula $\mathbf{f}_{\text{ext}} = \mathbf{0}$.

Since, the the variations \mathbf{v} are arbitrary, Eq. (26) leads to

$$\mathbf{f}(\mathbf{u}) := \mathbf{f}_{\text{int}} + \mathbf{f}_{\text{c}} - \mathbf{f}_{\text{ext}} = \mathbf{0}. \quad (27)$$

The global nodal force vectors in Eq. (27) are obtained from assembling the individual elemental contributions.

The elemental internal force vector $\mathbf{f}_{\text{int}}^e$ acting on element Ω^e is given as

$$\mathbf{f}_{\text{int}}^e = \int_{\Omega^e} \mathbf{B}_e^T \boldsymbol{\sigma} \, dv, \quad (28)$$

where \mathbf{B}_e is an array that contains the derivatives of the n_{ve} number of shape functions [61] and $\boldsymbol{\sigma}$ is the Cauchy stress tensor given by [57]

$$\boldsymbol{\sigma} = \frac{\Lambda}{J} (\ln J) \mathbf{I} + \frac{\mu}{J} (\mathbf{F}\mathbf{F}^T - \mathbf{I}), \quad (29)$$

and arranged in Voigt notation to suit Eq. (28). Introducing a modified shear modulus: $\mu^* := \mu - \Lambda \ln J$, the spatial elasticity tensor of the Neo-Hookean material can be written as

$$\mathbb{C} = \frac{\Lambda}{J} \mathbf{I} \otimes \mathbf{I} + \frac{2\mu^*}{J} \mathbb{I}, \quad (30)$$

where \mathbb{I} represents the fourth-order symmetric identity tensor, whose components can be expressed in terms of the Kronecker delta: $\mathbb{I}_{ijkl} = \frac{1}{2} (\delta_{ik}\delta_{jl} + \delta_{il}\delta_{jk})$.

The spatial elasticity tensor \mathbb{C} can be written in Voigt notation as

$$\mathbb{C}_v = \frac{1}{J} \begin{bmatrix} 2\mu^* + \Lambda & \Lambda & \Lambda & 0 & 0 & 0 \\ \Lambda & 2\mu^* + \Lambda & \Lambda & 0 & 0 & 0 \\ \Lambda & \Lambda & 2\mu^* + \Lambda & 0 & 0 & 0 \\ 0 & 0 & 0 & \mu^* & 0 & 0 \\ 0 & 0 & 0 & 0 & \mu^* & 0 \\ 0 & 0 & 0 & 0 & 0 & \mu^* \end{bmatrix} \quad (31)$$

The elemental contact force vector acting on $\partial_c \Omega^e$ is given as

$$\mathbf{f}_{\text{c}}^e = - \int_{\partial_c \Omega^e} \mathbf{N}_e^T \mathbf{t}_{\text{c}} \, da, \quad (32)$$

which can be transformed to the reference configuration using Nanson's formula,

$$\mathbf{n}_{\text{s}} \, da = J \mathbf{F}^{-T} \mathbf{N}_{\text{s}} \, dA, \quad (33)$$

where da denotes the surface element of the spatula with the orientation \mathbf{n}_{s} in the deformed configuration $\partial_c \Omega^e$, and dA denotes the corresponding surface element with the orientation \mathbf{N}_{s} in the undeformed reference configuration $\partial_c \Omega_0^e$. Then Eq. (32) becomes,

$$\mathbf{f}_{\text{c}}^e = - \int_{\partial_c \Omega_0^e} \mathbf{N}_e^T \Theta \mathbf{T}_{\text{c}} \, dA, \quad (34)$$

with

$$\Theta := -\mathbf{n}_p \cdot \mathbf{F}^{-T} \mathbf{N}_s, \quad (35)$$

where \mathbf{n}_p denotes the surface orientation of the substrate and is constant for the flat, rigid substrate considered in the current work. Also, for gecko adhesion Θ can be approximated as unity as shown by Sauer and Wriggers [33].

The elemental contact force vector in Eq. (34) can then be written as the sum of the contributions of the elemental force vectors due to normal adhesive traction \mathbf{T}_a and tangential frictional traction \mathbf{T}_f

$$\mathbf{f}_c^e = - \int_{\partial_c \Omega_e^e} \mathbf{N}_e^T \mathbf{T}_a \, dA - \int_{\partial_c \Omega_e^e} \mathbf{N}_e^T \mathbf{T}_f \, dA. \quad (36)$$

The nonlinear equation in Eq. (27), is solved iteratively using the Newton-Raphson method. Therefore, the tangent stiffness matrix \mathbf{k}_c^e is formed by the elemental contributions and is given by (see [33] for a detailed derivation)

$$\mathbf{k}_c^e = \frac{\partial \mathbf{f}_c^e}{\partial \mathbf{u}_e} = - \int_{\partial_c \Omega_e^e} \mathbf{N}_e^T \left(\frac{\partial \mathbf{T}_a}{\partial \mathbf{x}} + \frac{\partial \mathbf{T}_f}{\partial \mathbf{x}} \right) \mathbf{N}_e \, dA. \quad (37)$$

The derivatives of the adhesive and frictional tractions in Eq. (37) are given as

$$\frac{\partial \mathbf{T}_a}{\partial \mathbf{x}} = \frac{\partial T_a(r_s)}{\partial r_s} \mathbf{n}_p \otimes \mathbf{n}_p. \quad (38)$$

$$\frac{\partial \mathbf{T}_f}{\partial \mathbf{x}} = \begin{cases} -\varepsilon_T \mathbf{a}_p \otimes \mathbf{a}_p & \text{for elastic step i.e., sticking,} \\ \frac{\partial T_{\text{slide}}}{\partial r_s} \mathbf{n}_T \otimes \mathbf{a}_p & \text{for inelastic step i.e., sliding.} \end{cases} \quad (39)$$

3.2 Enrichment strategy

As discussed by Sauer [62], in solving a strip peeling problem for the case of strong adhesion, numerical difficulties arise because of the highly nonlinear nature of the van der Waals forces. For coarse finite element meshes, the use of four-noded quadrilateral elements can lead to poor convergence in the Newton-Raphson iterations. These issues can be resolved by using a very fine mesh, which lead to undesirably high computational cost. In order to address this issue, Sauer [62] introduced surface enriched FE based on p-refinement with fourth order Lagrange polynomials, denoted as Q1C4. This is employed in the current work. This means that, the contact elements of the spatula are discretized with Q1C4 finite elements whereas the bulk of the spatula domain is discretized using standard quadrilateral finite elements (denoted as Q1).

The formulation for Q1C4 elements is developed from standard Q1 elements for which the displacement fields in an element are given as $\mathbf{u}_e^h = \sum_{i=1}^4 N_i^0 \mathbf{u}_i$. The shape functions N_i^0 , for Q1 element, are given as

$$N_1^0(\xi, \eta) = \frac{1}{4}(1 - \xi)(1 - \eta), \quad (40)$$

$$N_2^0(\xi, \eta) = \frac{1}{4}(1 + \xi)(1 - \eta), \quad (41)$$

$$N_3^0(\xi, \eta) = \frac{1}{4}(1 + \xi)(1 + \eta), \quad (42)$$

$$N_4^0(\xi, \eta) = \frac{1}{4}(1 - \xi)(1 + \eta). \quad (43)$$

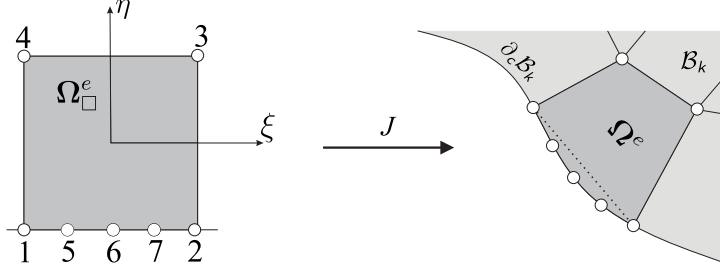


Figure 2: A schematic representation of Q1C4 enriched element and its corresponding mapping to physical space. (Adapted from Sauer [62])

In the formation of Q1C4, three extra nodes are inserted at $(\xi, \eta) = (0, -1)$, $(-0.5, -1)$, and $(0.5, -1)$ as shown in Figure 2, and the additional shape functions are defined as

$$N_5(\xi, \eta) = 2 \left(\xi^4 - \frac{5}{4}\xi^2 + \frac{1}{4} \right) (1 - \eta), \quad (44)$$

$$N_6(\xi, \eta) = -\frac{4}{3} \left(\xi^4 - \frac{1}{2}\xi^3 - \xi^2 + \frac{1}{2}\xi \right) (1 - \eta), \quad (45)$$

$$N_7(\xi, \eta) = -\frac{4}{3} \left(\xi^4 + \frac{1}{2}\xi^3 - \xi^2 - \frac{1}{2}\xi \right) (1 - \eta). \quad (46)$$

Then, with N_3^0 and N_4^0 remaining same, the following modified shape functions are obtained for the enriched surface element

$$N_1 = N_1^0 - \frac{1}{2}N_5 - \frac{3}{4}N_6 - \frac{1}{4}N_7, \quad (47)$$

$$N_2 = N_2^0 - \frac{1}{2}N_5 - \frac{1}{4}N_6 - \frac{3}{4}N_7. \quad (48)$$

With this, the displacement field in the interior of the surface element is interpolated as

$$\mathbf{u}_e^h = \sum_{i=1}^7 N_i \mathbf{u}_i. \quad (49)$$

4 Spatula Model

The spatula is modelled as a thin two-dimensional strip in plain strain, similar to many studies in the literature [17, 20, 39]. As such, the words “strip” and “spatula” are used interchangeably in the following text.

4.1 Model parameters

The dimensions of the strip are $L \times h$ (with $L = 200R_0$, $h = 10R_0$ where $R_0 = 1$ nm is introduced for normalization) as shown in Figure 3 [62]. The bottom 75% of the strip surface (“AE” in Figure 3) is assumed to be in adhesion. Hence, “AE” is assumed to represent the pad of the spatula while “EC” is assumed to represent the spatula shaft. The area of the gecko spatula pad is taken as, $A_{\text{pad}} = 49,524R_0^2$ [37]. Then the average width of the spatula pad becomes $w = 330.16R_0$.

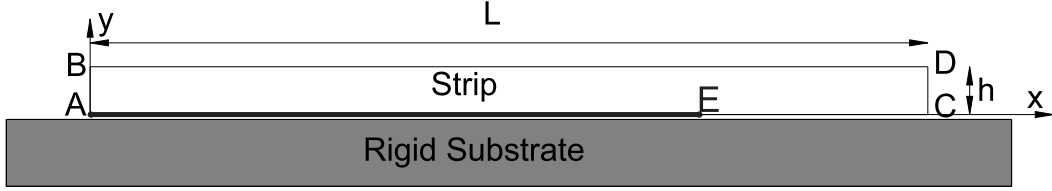


Figure 3: A deformable strip on a rigid substrate.

The material of the strip is taken to be an isotropic non-linear Neo-Hookean material (see Eq. 2). The default values for Young’s modulus and Poisson’s ratio are taken as $E = 2$ GPa and $\nu = 0.2$, respectively [17, 37]. The corresponding forces are calculated using Eqs. (10) and (15) with $r_0 = 0.4$ nm and $A_H = 10^{-19}$ J. The values considered for E , A_H , and r_0 correspond to the gecko spatula material and the associated adhesion energy [17, 37, 41]. This results in $\gamma_W = 25.266$ and $\gamma_L = 2.50$ according to Eq. (6). The friction coefficient is taken as $\mu_s = 0.3$ in agreement with experimental data on gecko seta friction on glass surfaces [5, 6, 46].

The strip is discretized into 240×12 quadrilateral finite elements along the x and y directions. Enriched contact finite elements, Q1C4, are used at the contact interface [62] and the bulk of the domain is discretized using standard quadrilateral finite elements. This particular finite element discretization has been shown to be very accurate for peeling computations [62]. Plane strain conditions are considered in all simulations.

4.2 Application of peeling

Peeling can occur in two ways: *tangentially-constrained* peeling and *tangentially-free* peeling. Next, each type is described.

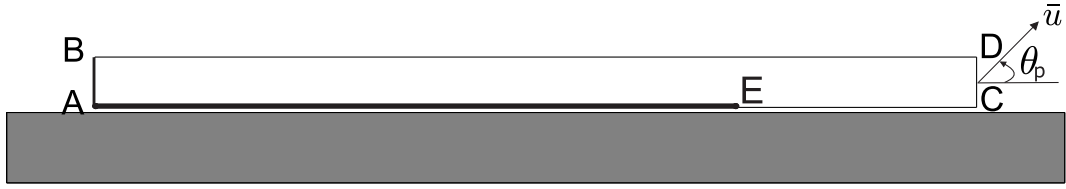
1. The *tangentially-constrained* peeling of the strip is effected by applying a displacement \bar{u} to the right end of the strip (CD) - resting in its initial configuration - at an angle, which is denoted as the peeling angle θ_p as shown in Figure 4a.

The displacement \bar{u} is applied such that $u_x = \bar{u} \cos(\theta_p)$ and $u_y = \bar{u} \sin(\theta_p)$. As a result, right end CD is constrained in the tangential direction. For a spatula, this essentially translates into constraining the tangential movement of the spatula shaft. Due to this, the direction of resultant force F_{res} is different from the applied displacement \bar{u} .

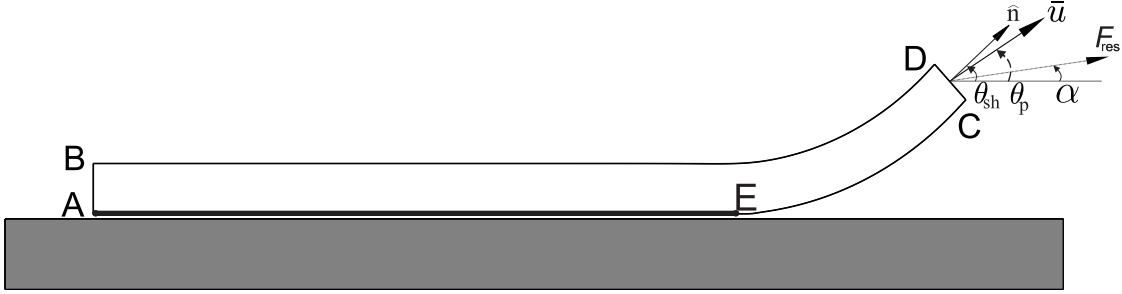
2. In case of *tangentially-free* peeling (examined in section 5.5), The displacement \bar{u} is applied only in the y-direction i.e. perpendicular to the substrate. As such, the lateral displacement of the shaft i.e. right end CD is not constrained. Hence the resultant force F_{res} is parallel to the applied displacement \bar{u} .

5 Results and Discussion

In this section the numerical results of the spatula peeling are presented. The normal (adhesive) and tangential (frictional) components of the resultant pull-off force F_{res} corresponding to the applied displacement \bar{u} are denoted by F_N and F_T , respectively. First, the numerical results for the case of *tangentially-constrained* peeling are presented and the effect of various parameters



(a) Peeling by applied displacement \bar{u} from the undeformed configuration. The inclination of \bar{u} , θ_p , is denoted as the peeling angle.



(b) Peeling by applied rotation θ and then applied displacement \bar{u} . Here, θ_{sh} denotes the angle between the cross-section normal \hat{n} and the substrate, while α denotes the angle between the resultant force F_{res} and the substrate.

Figure 4: Application of peeling.

– such as the peeling angle θ_p , shaft angle θ_{sh} , strip thickness h , and material stiffness – on the peeling behaviour is discussed in sections 5.1 to 5.4. It should be noted that for this type of peeling the resultant force angle α , which is the angle between the resultant force vector and the substrate, can be calculated as $\tan^{-1}(F_N/F_T)$ (see Figure 4b). The resultant force angle α is different from the peeling angle θ_p . This is due to the fact that the strip has non-zero bending stiffness and is restricted laterally as is noted in section 4.2. The results for the case of *tangentially-free* peeling are presented in section 5.5.

5.1 Description of the peeling curve

The peeling of the spatula from the substrate for any given peeling angle can be divided into two phases. This can be illustrated with the help of Figure 5, where the evolution of the normal pull-off force and the dimensionless strain energy (see Eq. (2)) with the applied displacement \bar{u} for $\theta_p = 60^\circ$ are shown. The first phase is from the point of zero pull-off force (denoted by “A”) to the maximum value of the pull-off force (denoted by “C”). The second phase is from point “C” to the point at which the spatula pad snaps-off from the substrate (denoted by “E”). The corresponding points on the strain energy curve are denoted by “a” to “e”. Figure 6 shows the strip deformation at the displacements marked in Figure 5.

In the first phase, the spatula remains in partial sticking contact and is being continuously stretched while peeling (Figures 6a and 6b). Moreover, in this phase, a part of the spatula pad behind the peeling front, that is still in contact, starts sliding as the spatula is pulled by the applied displacement. However, the rest of the spatula pad remains in sticking contact. This leads to stretching of the spatula, resulting in an increase in the stored strain energy of the spatula

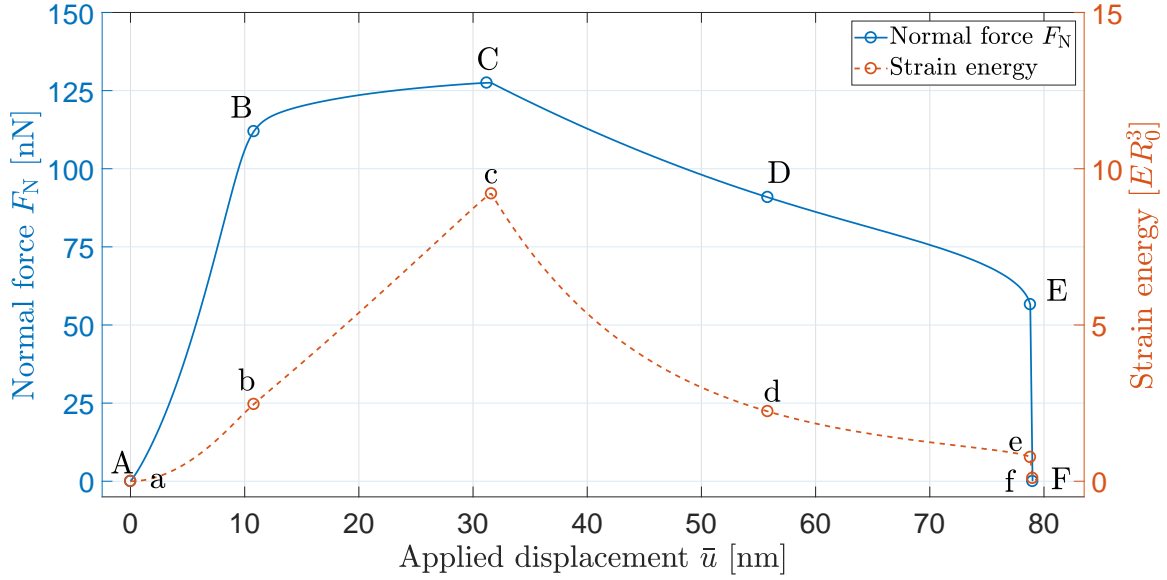


Figure 5: Evolution of the normal pull-off force F_N and strain energy (see Eq. (2)) with the applied displacement \bar{u} for peeling angle $\theta_p = 60^\circ$. Here, $ER_0^3 = 2 \text{ nN}\cdot\text{nm}$.

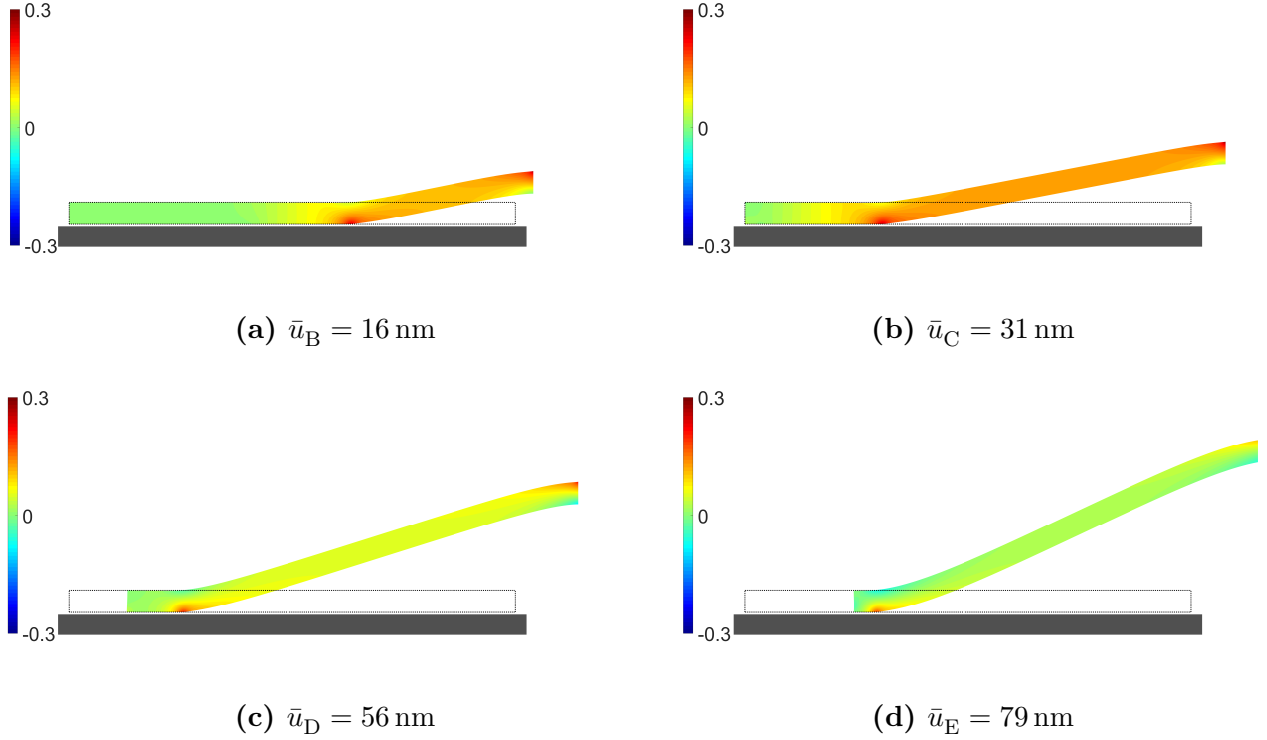


Figure 6: Deformed configurations of the strip for peeling angle $\theta_p = 60^\circ$ at the applied displacements \bar{u} marked in Figure 5 (B to E). Up to \bar{u}_C the spatula remains in partial sticking contact. Full sliding ensues beyond \bar{u}_C . The colorbar shows the normalised stresses $I_1/E = \text{tr}(\boldsymbol{\sigma})/E$.

as shown in Figure 5. As a result, this increases the force required to peel-off the spatula from the surface. After reaching the force maximum, the spatula pad is fully sliding during peeling

(Figures 6c and 6d). In this second phase, the strain energy that has been stored during the first phase, is gradually released (see Figure 5). As the displacement is applied beyond the point “e/E” the remaining part of the spatula pad immediately snaps-off from the surface releasing all the stored strain energy. At point “f/F” the spatula is completely peeled off the surface.

5.2 Influence of the peeling angle

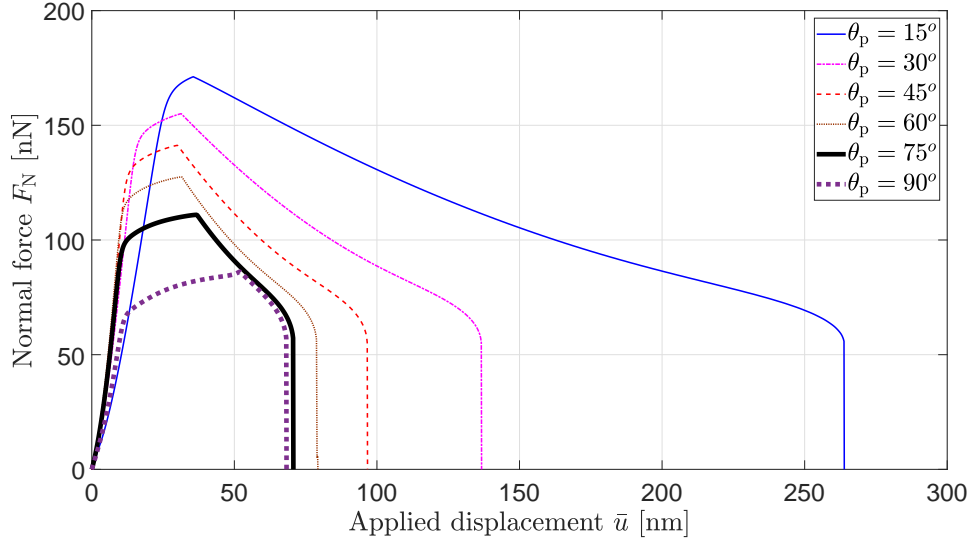


Figure 7: Evolution of the normal pull-off force F_N with the applied displacement \bar{u} for different peeling angles θ_p .

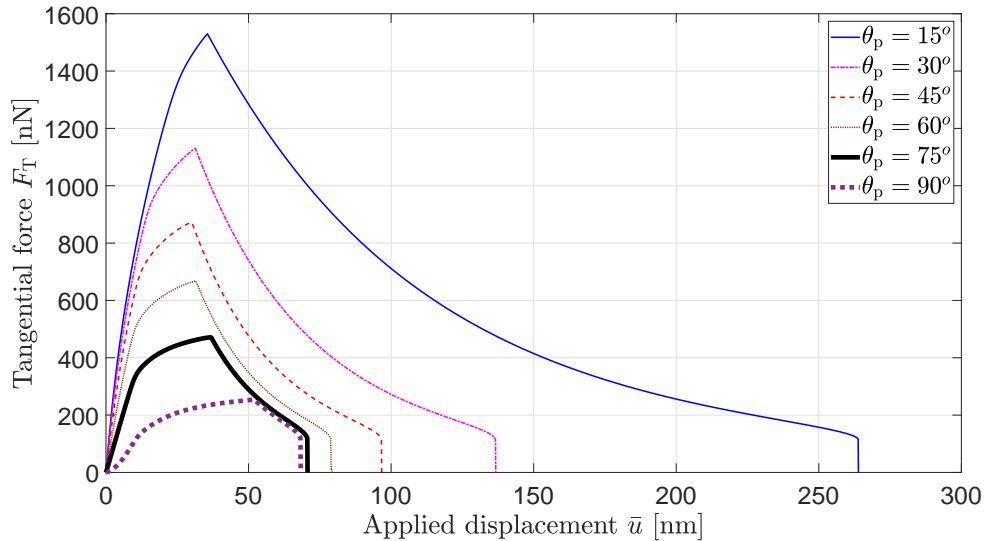


Figure 8: Evolution of the tangential pull-off force F_T with the applied displacement \bar{u} for different peeling angles θ_p .

The evolution of the normal (F_N) and tangential (F_T) (which is equal to the interfacial friction force F_f) components of the pull-off force with the applied displacement \bar{u} from initial configuration

is shown in Figures 7 and 8. For all cases, both normal and tangential force increase up to a maximum value, and then decrease after that, and this maximum value decreases with increasing peeling angle. This can also be seen from Figure 9, where the maximum values of the normal component F_N , tangential component F_T , and the resultant pull-off force F_{res} (occurring at point C in Figure 5) for different peeling angles are plotted. It can be observed that the friction force is the major contributor to the total force generated by the spatula. The maximum normal (F_N^{max}) and frictional force (F_T^{max}) values of approximately 174 nN and 1723 nN, respectively, are observed for $\theta_p = 10^\circ$.

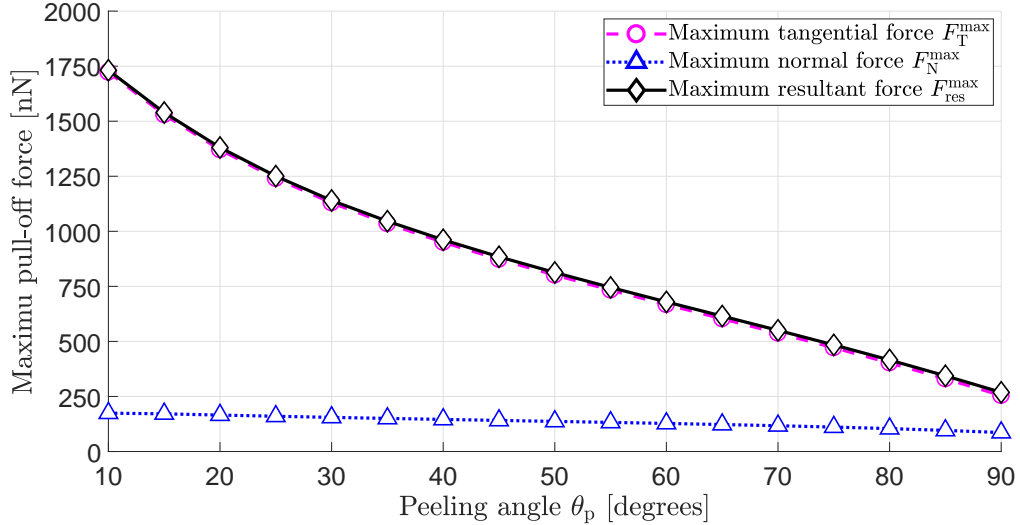


Figure 9: Evolution of the maximum pull-off force with peeling angle θ_p .

As mentioned in section 5.1, the stretching of the spatula increases the strain energy and, as seen in Figure 10, this increase is much higher when the spatula is pulled at low peeling angles as compared to high peeling angles. From these results combined with those in Figures 7, 8, and 9 it can be stated that the stretching of the spatula due to partial sliding close to the peel front leads to the increase in pull-off forces at small peeling angles. These results confirm the hypothesis of Labonte and Federle [23] that the partial sliding of the attached spatula pad could be one of the reasons for increased pull-off forces at small peeling angles. It should be noted that the curve for $\theta_p = 90^\circ$, as discussed in section 4.2, corresponds to *tangentially-constrained* peeling i.e. applying the displacement \bar{u} on the right end CD in the y-direction while it is constrained in the x-direction. This results in the generation of considerable friction forces. Hence, this is not equivalent to pulling the strip with a force acting perpendicular to the substrate, which implies zero friction forces.

5.2.1 Comparison with analytical models

The dependency of the maximum pull-off force on the corresponding force angle α (at point C in Figure 5) as obtained by the current model is compared with that of Kendall's peeling model [19] and the frictional sliding model of [27] in Figure 11. It can be observed that the current model predicts a similar trend as that of the other two models: the pull-off force is high for very low force angles and rapidly decreases as the force angle is increased. This behaviour is also consistent with experimental observations and other analytical models [17, 20, 63, 23]. However, the current

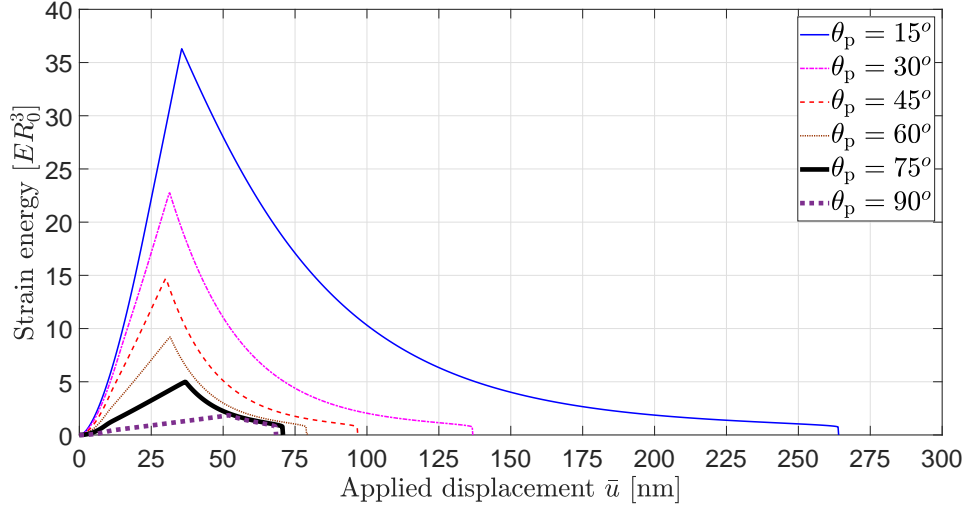


Figure 10: Evolution of the strain energy with the applied displacement \bar{u} for different peeling angles θ_p . Here, $ER_0^3 = 2 \text{ nN}\cdot\text{nm}$.

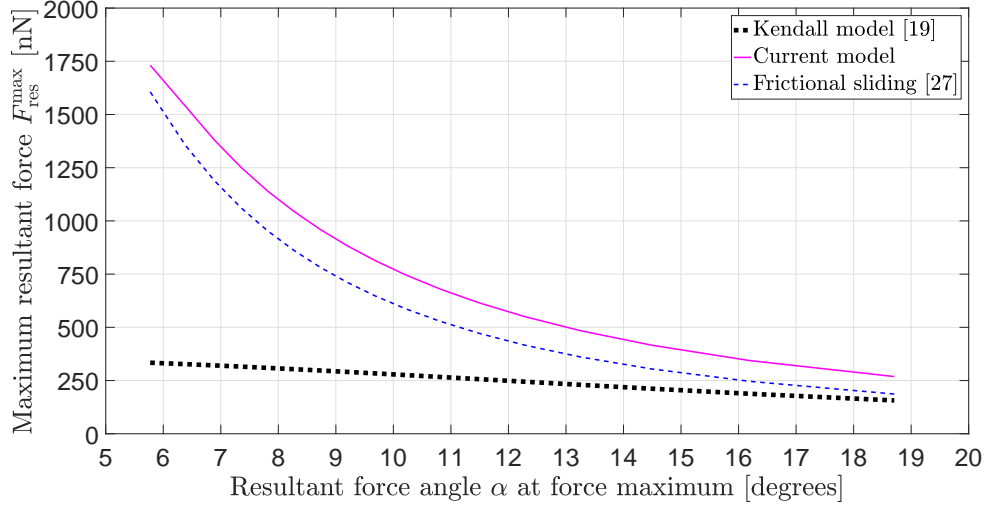


Figure 11: Comparison of different peeling models.

coupled adhesion-friction model predicts larger pull-off forces than those of Kendall’s [19] and the frictional sliding model of [27]. This is due to the non-zero bending stiffness of the strip.² Also, as α increases, all the three curves approach each other. However, even for vertical pulling i.e. $\alpha = 90^\circ$, the effect of non-zero bending stiffness still contributes to slightly larger pull-off forces and is discussed in section 5.4.

5.2.2 Estimation of the pull-off force at seta level

Although there have been no direct measurements of forces at the spatula level in the literature, Autumn et al. [5, 6] observed a maximum friction force of approximately $200 \mu\text{N}$ and a maximum normal force of $20\text{--}40 \text{ nN}$ for a single seta. Taking the number of spatulae per seta to be $100\text{--}1000$

²The non-zero bending stiffness implies a bending moment at end CD.

[17], the maximum friction and normal forces for a single spatula are estimated to be 200–2000 nN and 20 – 400 nN, respectively. The values, 1723 and 174 nN obtained here (see Figure 9), fit well within these ranges.

At first these maximum friction and adhesion forces obtained here might appear to be an overestimation when summed over the maximum limit of 1000 spatulae per seta. However, it can be observed from Figure 11, that these values correspond to a very low force angle $\alpha = 5.77^\circ$. Tian et al. [17] calculated a maximum friction force of 900 nN at a force angle close to $\alpha = 8^\circ$. The corresponding friction force obtained in the current work is 1139 nN. The difference between these observations can be attributed to the fact that in case of Tian et al. [17], the strip thickness is $h = 5$ nm and the friction coefficient $\mu_s = 0.2$. Whereas, the current results are for $h = 10$ nm and $\mu_s = 0.3$ and both of these parameters influence the pull-off forces. This is discussed in detail in section 5.4.1.

Moreover, when a seta attaches to a substrate after a perpendicular preload and parallel drag [5] it is not clear as to whether all the spatulae adhere to the surface or not. It is also doubtful that all the spatulae reach their force maximum at the same time. In the experiments of Huber et al. [16] only a fraction of all spatulae adhered to the substrate. This shows that not all the spatulae adhere even after a considerable parallel drag of the seta. This behaviour was also observed at the animal level by Eason et al. [63], who measured the stress distribution and contact area on the toes of geckos. They observed that the stress distribution is non-uniform owing to the fact that a significant portion of the setal arrays on the gecko toes did not adhere to the substrate. Moreover, even if all the spatulae are in contact with the substrate, it is not clear at what angles spatulae shafts are inclined and at what angles they experience pull-off forces. As it will be shown in section 5.3, the shaft angle significantly affects the maximum pull-off forces reached during peeling.

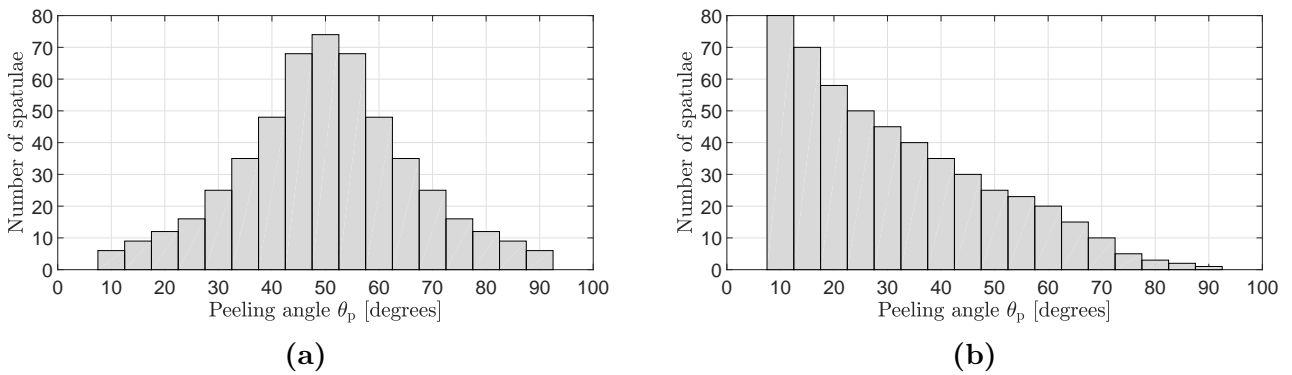


Figure 12: Assumed spatula distributions for different peeling angles.

Based on the setal density and branching characteristics, it is estimated that there are around 512 spatulae per seta [51]. To get an estimate of the total friction force per seta, two different spatula distributions are considered here. In the first distribution (Figure 12a), spatulae follow a normal distribution and experience the applied displacement \bar{u} at a mean angle of $\theta_p = 50^\circ$. By summing the maximum frictional forces per spatula at different peeling angles obtained in section 5.2 for this distribution, a total friction force of 422 μN per seta is obtained. Similarly, for the distribution in Figure 12b, in which 60% of total spatulae experience the applied displacement \bar{u} at angles $\leq 30^\circ$, the total friction force per seta is equal to 606 μN . However, these values correspond to the case when all the spatula are initially lying flat on the substrate i.e. $\theta_{sh} = 0^\circ$ and experiencing forces at very low angles $5^\circ - 20^\circ$. But, it is shown in section 5.3 the pull-off forces

are also affected by the angle at which the spatula shafts are inclined to the substrate. Changing the shaft angle from 0° to 90° decreases the pull-off forces by as much as close to 2.5 times. Hence, it is reasonable to conclude that the maximum frictional force of $200\ \mu\text{N}$ measured by Autumn et al. [5] has to be understood as the summation of all the spatulae interactions accounting for different spatulae inclinations and pulling angles. However, as pointed out by Puthoff et al. [51], it should be noted that the spatula distribution and the pull-off forces follow more sophisticated statistical principles than the rough estimates considered here.

5.3 Influence of the shaft angle

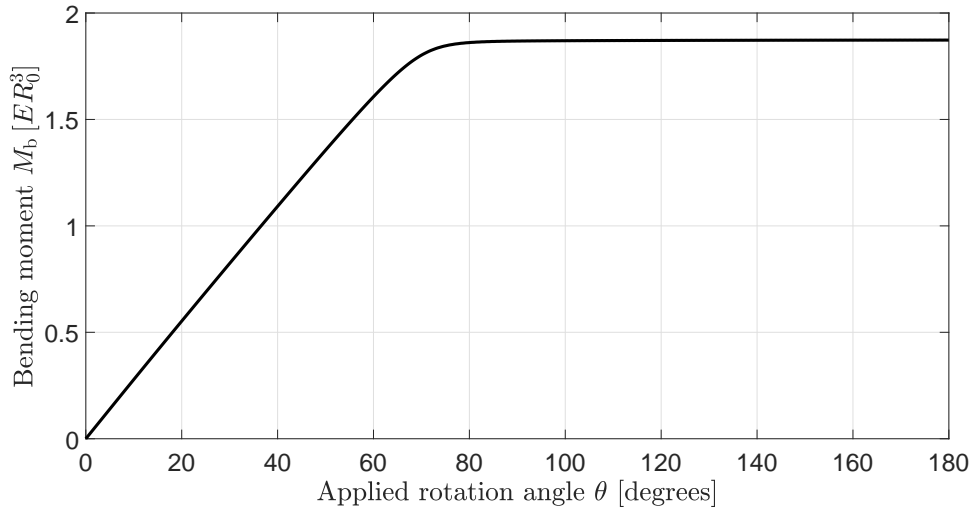


Figure 13: Evolution of the bending moment M_b with the applied rotation θ . Here, $ER_0^3 = 2\ \text{nN}\cdot\text{nm}$.

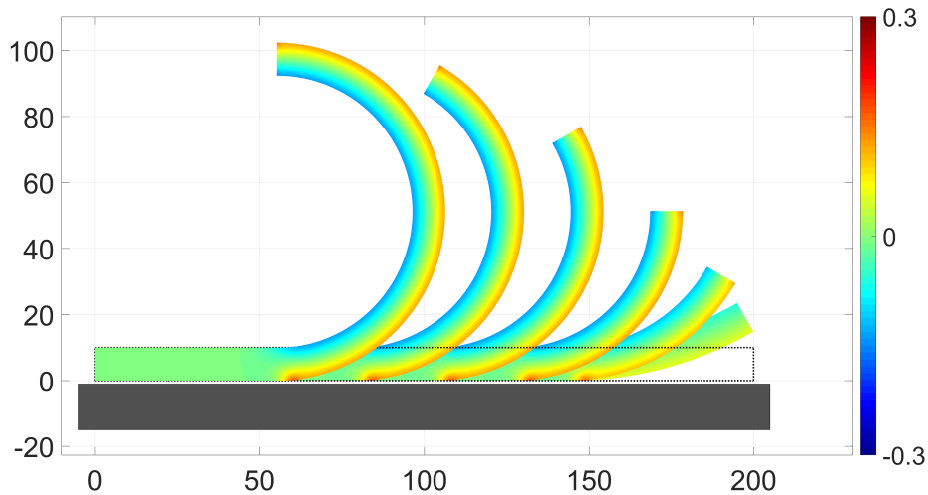


Figure 14: Deformed configurations of the strip for various rotation angles. The colorbar shows the normalised stresses $I_1/E = \text{tr}(\boldsymbol{\sigma})/E$.

In order to understand the influence of the shaft angle θ_{sh} on the pull-off forces, it is varied for

a given peeling angle θ_p . This is achieved by first applying the rotation angle θ_{sh} at the right end of the strip (CD), and then applying the displacement \bar{u} to that end at an angle θ_p , see Figure 4b.

Figure 13 shows the evolution of the bending moment M_b that is required to achieve the desired shaft angle $\theta = \theta_{sh}$. It can be observed that this bending moment reaches a constant value after a certain angle. The deformed configuration of the strip at different shaft angles is shown in Figure 14.

Once the desired spatula shaft angle is obtained, the spatula is peeled-off by applying a displacement at a peeling angle of $\theta_p = 90^\circ$. Figure 15 depicts the variation of the resultant pull-off forces for various spatula shaft angles. It can be observed that for a given peeling angle θ_p , the pull-off forces decrease as the spatula shaft angle increases. This is due to the fact that as the shaft angle increases, the spatula pad area that is still in contact with the substrate decreases as shown in Figure 14. As a result, the force that is required to detach the spatula from the substrate reduces. It can also be observed that the influence of the shaft angle is more pronounced for $\theta_{sh} > 60^\circ$, as the maximum force reached decreases more rapidly. This can also be understood by examining the deformed configurations in Figure 14. Here, it is clear that there is not much change in the spatula pad area for small shaft angle. It is only after $\theta_{sh} > 60^\circ$ that the spatula pad area still-in-contact reduces more rapidly.

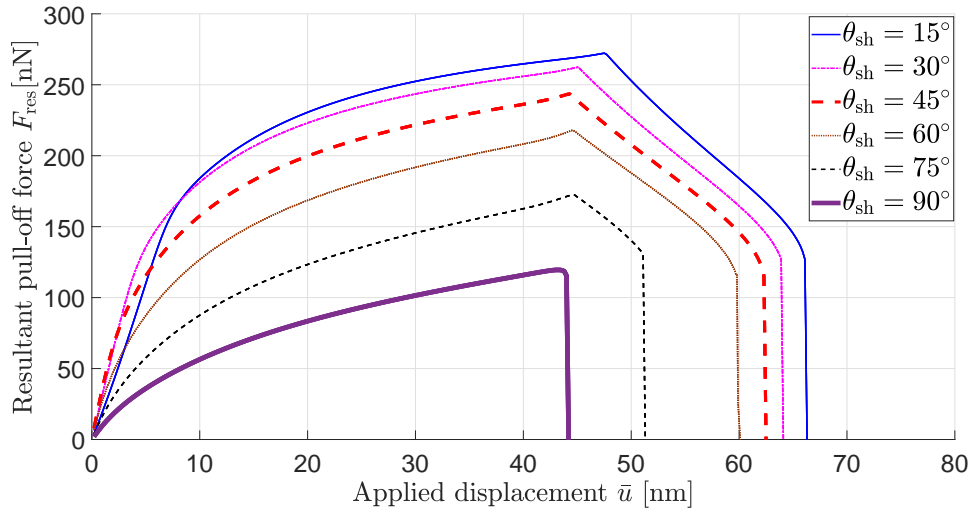


Figure 15: Evolution of the resultant pull-off force F_{res} with the applied displacement \bar{u} for different shaft angles θ_{sh} and peeling angle $\theta_p = 90^\circ$.

5.4 Influence of bending stiffness

In this section the influence of bending stiffness on the pull-off forces is studied by varying the strip thickness h and the material stiffness E (via material parameter γ_w).

5.4.1 Strip thickness

Figure 16 shows the influence of the spatula thickness h on the variation of the maximum resultant pull-off forces with peeling angle θ_p . It can be observed that as the thickness increases the maximum pull-off force achieved during the peeling increases. As the thickness increases, the bending stiffness of the spatula increases and a higher force is needed to peel the spatula from

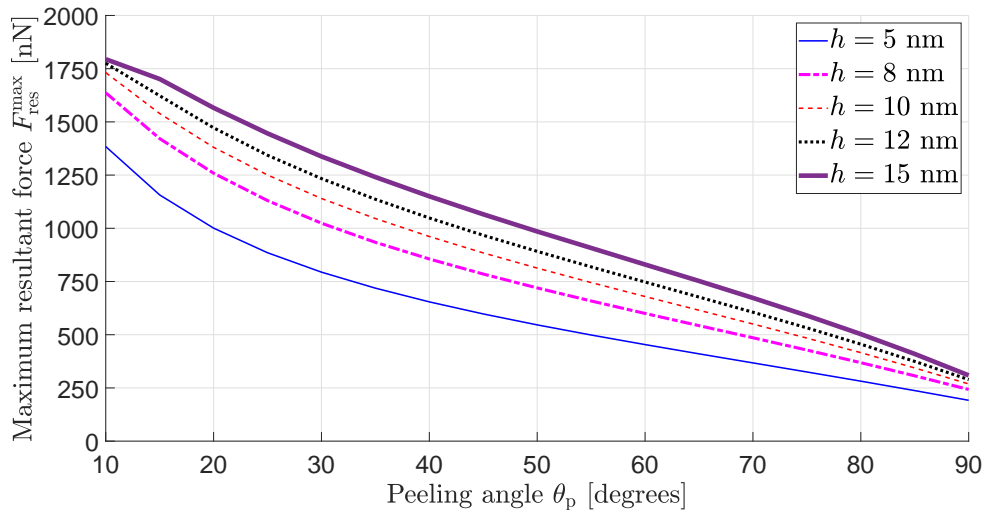


Figure 16: Evolution of the maximum resultant pull-off force $F_{\text{res}}^{\text{max}}$ with the peeling angle θ_p for different strip thicknesses.

the substrate. However, as observed from Figure 16, this increase in the pull-off force is more significant for low h than for high h . This is clear from the fact that the minimum increase in the pull-off force for $h = 5$ to $h = 10$ nm is equal to 25%, whereas the maximum increase in pull-off force is only 22% for the increase $h = 10$ to $h = 15$ nm. At first, this increase in adhesion with spatula thickness might lead us to conclude that a large thickness is preferred. Geckos generate a large amount of friction and adhesion by increasing the area of contact with the help of the large number of thin spatulae. Although increasing the spatula thickness generates more adhesive forces, it also increases the volume (and mass) of the gecko body faster than the increase in the surface area [64] which for a dynamic species like gecko is undesirable. Rizzo et al. [65], in their investigation of the gecko spatula with an electron microscope, observed that the thickness of the gecko spatula pad is only 5 – 10 nm. It has also been suggested by Persson and Gorb [64] that the spatula pad thickness needs to be approximately 5 – 10 nm, in order for it to be compliant enough to adhere to a variety of substrates which in nature are mostly rough.

5.4.2 Material stiffness

Geckos inhabit a wide range of environments such as tropics, urban, and deserts. As such, they have to endure changes in geographical and atmospheric conditions such as the temperature, wetness, and relative humidity (moisture) [70]. It has been experimentally observed that the humidity greatly affects the mechanical properties of gecko setae [68, 69, 70]. Prowse et al. [69] observed that at 80% relative humidity (RH), the complex elastic modulus E^{*3} of a single gecko decreased to one-third of its value at dry conditions. The elastic modulus E has been found to decrease by a factor of 1.73 when RH increased from 30% to 80% i.e. the seta material becomes softer. This has been observed to affect the adhesion capabilities of the geckos [68]. Hence, it would be helpful to study how these changes in mechanical properties affect the adhesion behaviour using the current computational model.

The variation of the maximum resultant pull-off force with peeling angle θ_p for different values

³ $|E^*| = \sqrt{(E')^2 + (E'')^2}$, where E' and E'' denote the storage and loss moduli, respectively.

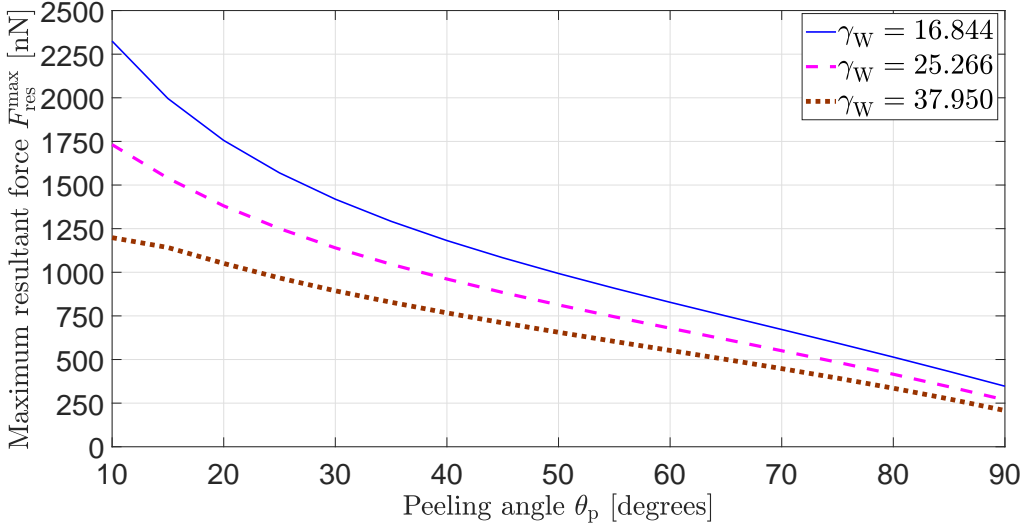


Figure 17: Evolution of the maximum resultant pull-off force F_{res}^{max} with the peeling angle θ_p for different material stiffness.

of material stiffness E is shown in Figure 17. This is achieved by changing the material parameter γ_W . From the definition in Eq. (6), it is clear that an increase in γ_W corresponds to an increase in the material stiffness. It can be seen that as the material stiffness decreases the pull-off force increases. This is due to the fact that as the stiffness decreases, the spatula becomes more compliant and adheres to the substrate more readily. This is illustrated in Figure 18. Here, it can be seen that at a given shaft angle of $\theta_{sh} = 90^\circ$, the strip with lower material stiffness has more pad area that is still in contact with the substrate. Moreover, the stress developed at the peeling front increases as the material stiffness decreases. Hence, the force required to peel off the spatula increases. The current results allow for a better insight into this complex system, which in turn allows for designing better gecko inspired synthetic adhesives.

5.5 Vertical pulling and spatula detachment

Despite generating high attachment forces, geckos can detach from a substrate in just 20 ms and with very small force [66]. However, for the case of *tangentially-constrained* peeling discussed so far, it can be observed that at the point of detachment (shown by point “e/E” in Figure 5) the pull-off forces are still quite high (see Figures 7 and 8). So, in order to facilitate quick detachment with small force, the frictional forces should vanish. This can be achieved through *tangentially-free* peeling as described in section 4.2. As the spatula is pulled perpendicular to the substrate, this type of peeling is referred to as “vertical pulling” here.

The evolution of the corresponding resultant forces with the applied displacement \bar{u} for various shaft angles θ_{sh} is plotted in Figure 19. For this case, the tangential forces are zero by design. It can also be observed that, as the shaft angle increases, the maximum pull-off force decreases. This is similar to the behaviour observed in section 5.3 for *tangentially-constrained* peeling. The maximum pull-off force is lowest for $\theta_{sh} = 90^\circ$ and is equal to 12.62 nN. This value is close to the value of 10 nN observed by Huber et al. [16] in their experiments, where the spatulae shafts are inclined at 90° and are pulled vertically. This result is also within the range of 2 – 16 nN obtained experimentally by Sun et al. [67] for vertical pulling of the spatula. These results also match

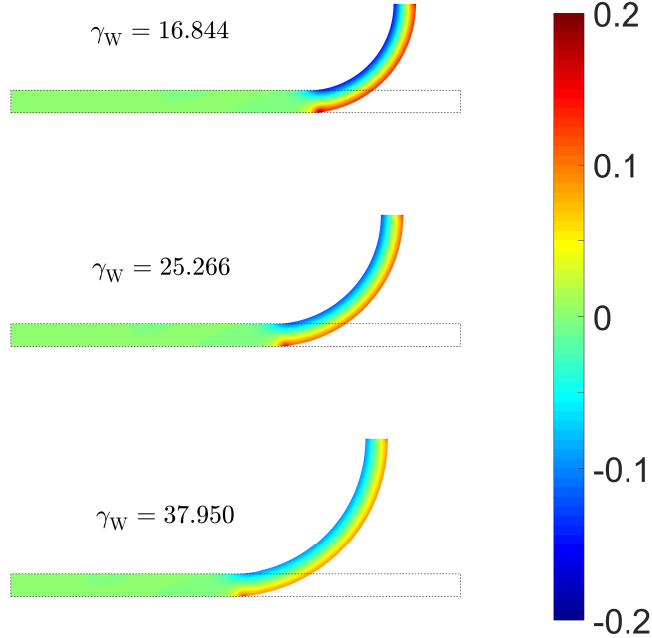


Figure 18: Deformation and stress for different material stiffness for a rotated configuration of $\theta_{\text{sh}} = 90^\circ$. The colorbar shows the normalised stresses $I_1/E = \text{tr}(\boldsymbol{\sigma})/E$.

well with the beam results of Sauer [38]. Therefore, gecko spatulae can detach with very small amount of force by changing the shaft angle θ_{sh} to 90° and then peel like a tape perpendicular to the substrate as shown in Figure 20.

It has been observed that during the attachment step, geckos perform a roll in action to grip their toes when they adhere to a substrate and they peel off their toes while detaching (which is called digital hyperextension) [6, 11]. The gripping action causes the setae to slide very slightly and brings the spatulae in contact with the substrate. At the same time, this gripping action also changes the angle between the setal shaft and the substrate, which in turn decreases the angle between the spatula shaft and the substrate [17]. This dragging at a low angle causes the spatulae to stretch [20, 40], increasing the stored strain energy (see Figures 5 and 10). This corresponds to *tangentially-constrained* peeling: As shown in sections 5.1 to 5.4 (see Figures 7 to 11) the spatulae stretch and very high maximum pull-off forces are reached at small resultant force angles. Similarly, when the gecko hyperextends its toes to disengage from the substrate this again changes the angle between the seta shaft and the substrate. Rolling out the toes results in a lever action of the setal shafts as described by Tian et al. [17]. Autumn et al. [46] observed that the seta spontaneously detaches from the substrate when the angle between seta shaft and the substrate increases above 30° . At the spatula level, these actions increase the angle between the spatula shaft and the substrate to 90° and one by one each spatula disengages from the substrate. This spatula disengagement corresponds to *tangentially-free* peeling: As seen from the results in Figure 19 this action requires very small amount of force.

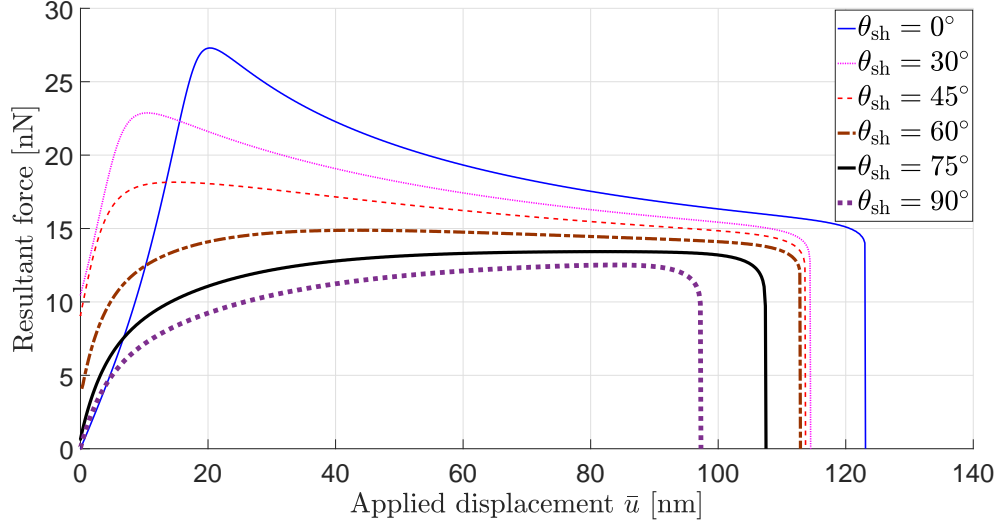


Figure 19: Evolution of the resultant pull-off force $F_{\text{res}} = F_N$ with the applied displacement \bar{u} for different shaft angles θ_{sh} for vertical pulling (where $F_T = 0$).

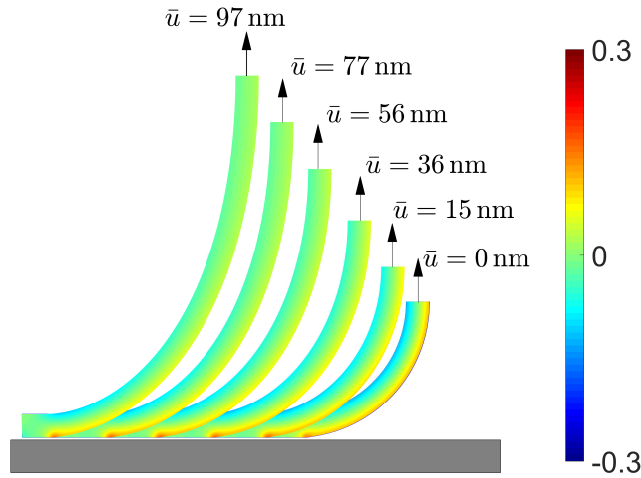


Figure 20: Deformed configurations of the strip for vertical pulling with $\theta_{\text{sh}} = 90^\circ$ at various applied displacements \bar{u} . The colorbar shows the normalised stresses $I_1/E = \text{tr}(\boldsymbol{\sigma})/E$.

6 Conclusions

Peeling of gecko spatulae is studied using a two-dimensional strip model. A continuum-based coupled adhesion-friction formulation implemented within a nonlinear finite element framework is employed to investigate the peeling behaviour of the spatula. It is shown that during peeling, the spatula stretches due to partial sliding of the spatula pad at the peel front leading to an increase in the strain energy of the spatula. This in turn increases the amount of maximum pull-off force required to detach the spatula from the substrate. The influence of different parameters on the *tangentially-constrained* peeling of the spatula is also investigated in the present work. The results are summarized in Table 1. Further, using *tangentially-free* peeling, it is shown that the easy detachment of the spatula is facilitated by changing the spatula shaft angle and then pulling vertically. The current computational model is not limited by the geometrical, kinematical, and material restrictions of theoretical models. As such, it can be employed in the future to study rate effects, seta peeling, and peeling of other biological adhesive systems.

Table 1: Influence of different parameters on the pull-off forces in *tangentially-constrained* peeling.

No.	Parameter	Variation	Pull-off forces
1.	Peeling angle θ_p	decreases	increases
2.	Shaft angle θ_{sh}	decreases	increases
3.	Strip thickness h	decreases	decreases
4.	Material stiffness E	decreases	increases

Acknowledgement

S.G. and S.S.G. are grateful to the SERB, DST for supporting this research under project SR/FTP/ETA-0008/2014. R.A.S. is grateful to the German Research foundation (DFG) for supporting the research under project GSC 111. The authors thank Dr. David Labonte for his valuable comments.

References

- [1] Scherge, M.; Gorb, S. *Biological Micro- and Nanotribology*. NanoScience and Technology. Springer Berlin Heidelberg, Berlin, Heidelberg, 2001.
- [2] Ruibal, R.; Ernst, V. The structure of the digital setae of lizards. *J. Morphol.* **1965**, 117, 271–293. DOI:10.1002/jmor.1051170302.
- [3] Niederegger, S.; Gorb, S.-N. Friction and adhesion in the tarsal and metatarsal scopulae of spiders. *J. Comp. Physiol. A.* **2006**, 192, 1223–1232. DOI:10.1007/s00359-006-0157-y.
- [4] Hiller, U. Correlation between corona-discharge of polyethylene-films and the adhering power of *Tarentola M. mauritanica* (Rept.). *Forma et functiol.* **1969**, 117, 350352.
- [5] Autumn, K.; Liang, Y. A.; Hsieh, S. T.; Zesch, W.; Chan, W. P.; Kenny, T. W.; Fearing, R.; Full, R. J. Adhesive force of a single gecko foot-hair. *Nature.* **2000**, 405, 681–684. DOI:10.1038/35015073.

- [6] Autumn, K.; Sitti, M.; Liang, Y. A.; Peattie, A. M.; Hansen, W. R.; Sponberg, S.; Kenny, T. W.; Fearing, R.; Israelachvili, J. N.; Full, R. J. Evidence for van der Waals adhesion in gecko setae. *Proc. Natl. Acad. Sci.* **2002**, 99, 12252–12256. DOI:10.1073/pnas.192252799.
- [7] Russell, A. P.; Integrative Functional Morphology of the Gekkotan Adhesive System (Reptilia: Gekkota). *Integr. Comp. Biol.* **2002**, 42, 1154–1163. DOI:10.1093/icb/42.6.1154.
- [8] Autumn, K. Gecko adhesion: Structure, function, and applications. *MRS Bull.* **2007**, 32, 473–478. DOI:10.1557/mrs2007.80.
- [9] Pugno, N. M. Spiderman gloves. *Nano Today.* **2008**, 3, 35–41. DOI:10.1016/S1748-0132(08)70063-X.
- [10] Asbeck, A.; Dastoor, S.; Parness, A.; Fullerton, L.; Esparza, N.; Soto, D.; Heyneman, B.; Cutkosky, M. Climbing rough vertical surfaces with hierarchical directional adhesion. In *Proc. - IEEE Int. Conf. Robot. Autom.* 2675–2680, 2009.
- [11] Hu, S.; Lopez, S.; Niewiarowski, P. H.; Xia, Z. Dynamic self-cleaning in gecko setae via digital hyperextension. *J. R. Soc. Interface.* **2012**, 9, 2781–2790. DOI:10.1098/rsif.2012.0108.
- [12] Drotlef, D. M.; Amjadi, M.; Yunusa, Md.; Sitti, M. Bioinspired Composite Microfibers for Skin Adhesion and Signal Amplification of Wearable Sensors. *Adv. Mater.* **2017**, 29, 1701353–1—1701353–8. DOI:10.1002/adma.201701353.
- [13] Hou, X.; Su, Y.; Jiang, S.; Li, L.; Chen, T.; Sun, L.; Deng, Z. Adhesion mechanism of space-climbing robot based on discrete element and dynamics. *Adv. Mech. Eng.* **2018**, 10, 1–15. DOI:10.1177/1687814018772934.
- [14] Sitti, M.; Fearing, R. S. Synthetic gecko foot-hair micro/nano-structures as dry adhesives. *J. Adhes. Sci. Technol.* **2003**, 17, 1055–1073. DOI:10.1163/156856103322113788.
- [15] Gao, H.; Wang, X.; Yao, H.; Gorb, S.; Arzt, E. Mechanics of hierarchical adhesion structures of geckos. *Mech. Mater.* **2005**, 37, 275–285. DOI:10.1016/j.mechmat.2004.03.008.
- [16] Huber, G.; Gorb, S. N.; Spolenak, R.; Arzt, E. Resolving the nanoscale adhesion of individual gecko spatulae by atomic force microscopy. *Biol. Lett.* **2005**, 1, 2–4. DOI:10.1098/rsbl.2004.0254.
- [17] Tian, Y. Pesika, N.; Zeng, H.; Rosenberg, K.; Zhao, B.; McGuiggan, P.; Autumn, K.; Israelachvili, J. N. Adhesion and friction in gecko toe attachment and detachment. *Proc. Natl. Acad. Sci.* **2006**, 103, 19320–19325. DOI:10.1073/pnas.0608841103.
- [18] Pesika, N. S.; Tian, Y.; Zhao, B.; Rosenberg, K.; Zeng, H.; McGuiggan, P.; Autumn, K.; Israelachvili, J.-N. Peel-Zone Model of Tape Peeling Based on the Gecko Adhesive System. *J. Adhes.* **2007**, 83, 383–401. DOI:10.1080/00218460701282539.
- [19] Kendall, K. Thin-film peeling—the elastic term. *J. Phys. D. Appl. Phys.* **1975**, 8, 1449–1452. DOI:10.1088/0022-3727/8/13/005.
- [20] Chen, B.; Wu, P.; Gao, H. Pre-tension generates strongly reversible adhesion of a spatula pad on substrate. *J. R. Soc. Interface* **2009**, 6, 529–537. DOI:10.1098/rsif.2008.0322.

- [21] Begley, M. R.; Collino, R. R.; Israelachvili, J. N.; McMeeking, R. M. Peeling of a tape with large deformations and frictional sliding. *J. Mech. Phys. Solid.* **2013**, 61, 1265–1279. DOI:10.1016/j.jmps.2012.09.014
- [22] Peng, Z.; Chen, S. Effect of bending stiffness on the peeling behaviour of an elastic thin film on a rigid substrate. *Phys. Rev. E* **2015**, 91, 042401. DOI:10.1016/j.ijsostr.2014.10.011.
- [23] Labonte, D.; Federle, W. Biomechanics of shear-sensitive adhesion in climbing animals: peeling, pre-tension and sliding-induced changes in interface strength. *J. R. Soc. Interface* **2016**, 13, 20160373. DOI:10.1098/rsif.2016.0373
- [24] Kim, J. K.; Varenberg, M. Biomimetic wall-shaped adhesive microstructure for shear-induced attachment: the effects of pulling angle and preliminary displacement. *J. R. Soc. Interface* **2017**, 1420170832. DOI:10.1098/rsif.2017.0832
- [25] Peng, Z.; Yin, H.; Yao, Y.; Chen, S. Effect of thin-film length on the peeling behaviour of film-substrate interfaces. *Phy. Rev. E* **2019**, 100, 032804. DOI:10.1103/PhysRevE.100.032804
- [26] Kwak, J. S.; Kim, T. W. A review of adhesion and friction models for gecko feet. *Int. J. Precis. Eng. Manuf.* **2010**, 11, 171–186. DOI:10.1007/s12541-010-0020-5.
- [27] Jagota, A.; Hui, C. H. Adhesion, friction, and compliance of bio-mimetic and bio-inspired structured interfaces. *Mater. Sci. Eng. R Reports* **2011**, 72, 253–292. DOI:10.1016/j.mser.2011.08.001.
- [28] Zhou, M.; Pesika, N.; Zeng, H.; Tian, Y.; Israelachvili, J. Recent advances in gecko adhesion and friction mechanisms and development of gecko-inspired dry adhesive surfaces. *Friction.* **2013**, 1, 114–129. DOI:10.1007/s40544-013-0011-5.
- [29] Kasar, A. K.; Ramachandran, R.; Menezes, P.-L. Natural Adhesion System Leads to Synthetic Adhesives. *J. Bio- Tribo-Corrosion.* **2018**, 4, 1–17. DOI:10.1007/s40735-018-0160-1.
- [30] Seale, M.; Cummins, C.; Viola, I.M.; Mastropaolo, E.; and Nakayama, N. Design principles of hair-like structures as biological machines. *J. R. Soc. Interface.* **2018**, 15, 20180206. DOI:10.1098/rsif.2018.0206.
- [31] Russell, A. P.; Stark, A. Y.; Higham, T. E. The Integrative Biology of Gecko Adhesion: Historical Review, Current Understanding, and Grand Challenges. *Integr. Comp. Biol.* **2019**, 59, 101–116. DOI:10.1093/icb/icz032.
- [32] Federle, W.; Labonte, D. Dynamic biological adhesion: mechanisms for controlling attachment during locomotion. *Phil. Trans. R. Soc. B* **2019**, 374, 20190199. DOI:10.1098/rstb.2019.0199
- [33] Sauer, R. A.; Wriggers, P. Formulation and analysis of a three-dimensional finite element implementation for adhesive contact at the nanoscale. *Comput. Methods Appl. Mech. Eng.* **2009**, 198, 3871–3883. DOI:10.1016/j.cma.2009.08.019.
- [34] Sauer, R. A. Multiscale modelling and simulation of the deformation and adhesion of a single gecko seta. *Comput. Methods Biomech. Biomed. Engin.* **2009**, 12, 627–640. DOI:10.1080/10255840902802917.

- [35] Sauer, R. A. A computational model for nanoscale adhesion between deformable solids and its application to gecko adhesion. *J. Adh. Sci. Tech.* **2010**, 24, 1807–1818. DOI:10.1163/016942410X507588.
- [36] Sauer, R. A.; Li, S. A contact mechanics model for quasi-continua. *Int. J. Numer. Methods Eng.* **2007**, 71, 931–962. DOI:10.1002/nme.1970.
- [37] Sauer, R. A.; Holl, M. A detailed 3D finite element analysis of the peeling behaviour of a gecko spatula. *Comput. Methods Biomech. Biomed. Engin.* **2013**, 16, 577–591. DOI:10.1080/10255842.2011.628944.
- [38] Sauer, R. A. The peeling behaviour of thin films with finite bending stiffness and the implications on gecko adhesion. *J. Adhes.* **2011**, 87, 624–643.
- [39] Peng, Z. L.; Chen, S. H.; Soh, A. K. Peeling behaviour of a bio-inspired nano-film on a substrate. *Int. J. Solids Struct.* **2010**, 47, 1952–1960. DOI:10.1016/j.ijsolstr.2010.03.035.
- [40] Cheng, Q. H.; Chen, B.; Gao, H. J.; Zhang, Y. W. Sliding-induced non-uniform pretension governs robust and reversible adhesion: a revisit of adhesion mechanisms of geckos. *J. R. Soc. Interface* **2012**, 9, 283–291. DOI:10.1098/rsif.2011.0254.
- [41] Gautam, S. S.; Sauer, R. A. A composite time integration scheme for dynamic adhesion and its application to gecko spatula peeling. *Int. J. Comput. Methods.* **2014**, 11, 1350104. DOI:10.1142/S0219876213501041.
- [42] Sauer, R. A.; Mergel, J. C. A geometrically exact finite beam element formulation for thin film adhesion and debonding. *Finite Elem. Anal. Des.* **2014**, 86, 120–135. DOI:10.1016/j.finel.2014.03.009.
- [43] Mergel, J. C.; Sauer, R. A.; Saxena, A. Computational optimization of adhesive microstructures based on a nonlinear beam formulation. *Struct. Multidiscip. Optim.* **2014**, 50, 1001–1017. DOI:10.1007/s00158-014-1091-1.
- [44] Mergel, J. C.; Sauer, R. A. On the optimum shape of thin adhesive strips for various peeling directions. *J. Adhes.* **2014**, 90, 526–544. DOI:10.1080/00218464.2013.840538.
- [45] Sauer, R. A. A survey of computational models for adhesion. *J. Adhes.* **2016**, 92, 81–120. DOI:10.1080/00218464.2014.1003210.
- [46] Autumn, K.; Dittmore, A.; Santos, D.; Spenko, M.; Cutkosky, M. Frictional adhesion: a new angle on gecko attachment. *J. Exp. Biol.* **2006**, 209, 3569–3579. DOI:10.1242/jeb.02486.
- [47] Nosonovsky, M.; Bhushan, B. Multiscale friction mechanisms and hierarchical surfaces in nano- and bio-tribology. *Mater. Sci. Eng. R Reports.* **2007**, 58, 162–193. DOI:10.1016/j.mser.2007.09.001.
- [48] Derjaguin, B. Molekulartheorie der äußeren Reibung. *Zeitschrift für Phys.* **1934**, 88, 661–675. DOI:10.1007/BF01333114.

- [49] Majidi, C.; Groff, R.-E.; Maeno, Y.; Schubert, B.; Baek, S.; Bush, B.; Maboudian, R.; Gravish, N.; Wilkinson, M.; Autumn, K.; Fearing, R.-S.; et al. High Friction from a Stiff Polymer Using Microfiber Arrays. *Phys. Rev. Lett.* **2006**, 97, 076103–1—076103–4. DOI:10.1103/PhysRevLett.97.076103.
- [50] Gravish, N.; Wilkinson, M.; Sponberg, S.; Parness, A.; Esparza, N.; Soto, D.; Yamaguchi, T.; Broide, M.; Cutkosky, M.; Creton, C.; Autumn, K.; et al. Rate-dependent frictional adhesion in natural and synthetic gecko setae. *J. R. Soc. Interface.* **2010**, 7, 259–269. DOI:10.1098/rsif.2009.0133.
- [51] Puthoff, J. B.; Holbrook, M.; Wilkinson, M. J.; Jin, K.; Pesika, N. S.; Autumn, K. Dynamic friction in natural and synthetic gecko setal arrays. *Soft Matt.* **2013**, 9, 4855–4863. DOI:10.1039/c3sm50267h.
- [52] Jiang, J. W.; Park, H. S. A Gaussian treatment for the friction issue of Lennard-Jones potential in layered materials: Application to friction between graphene, MoS₂, and black phosphorus. *J. Appl. Phys.* **2015**, 117, 124304–1–124304–8. DOI:10.1063/1.4916538.
- [53] Del Piero, G.; Raous, M. A unified model for adhesive interfaces with damage, viscosity, and friction. *Eur. J. Mech. - A/Solids.* **2010**, 29, 496–507. DOI:10.1016/j.euromechsol.2010.02.004.
- [54] Snozzi, L.; Molinari, J. F. A cohesive element model for mixed mode loading with frictional contact capability. *Int. J. Numer. Methods Eng.* **2013**, 93, 510–526. DOI:10.1002/nme.4398.
- [55] Cocou, M.; Schryve, M.; Raous, M.; A dynamic unilateral contact problem with adhesion and friction in viscoelasticity. *Zeitschrift für Angew. Math. und Phys.* **2010**, 61, 721–743. DOI:10.1007/s00033-009-0027-x.
- [56] Mergel, J. C.; Sahli, R.; Scheibert, J.; Sauer, R. A. Continuum contact models for coupled adhesion and friction. *J. Adhes.* **2018**, 95, 1101–1133. DOI:10.1080/00218464.2018.1479258.
- [57] Bonet, J.; Wood, R.-D. *Nonlinear Continuum Mechanics for Finite Element Analysis*, 2nd ed.; Cambridge University Press; 2008.
- [58] Israelachvili, J. N. *Intermolecular and Surface Forces*, 3rd ed; Elsevier; 2011.
- [59] Tabor, D. Surface forces and surface interactions. *J. Coll. Inter. Sci.* **1977**, 58, 2–13. DOI:10.1016/0021-9797(77)90366-6.
- [60] Wriggers, P. *Computational Contact Mechanics*. Springer: Berlin, Heidelberg, 2006.
- [61] Zienkiewicz, O.; Taylor, R.; Zhu, J. *The finite element method: Its basis and fundamentals*. Seventh Edition. Butterworth-Heinemann, 2013.
- [62] Sauer, R. A. Enriched contact finite elements for stable peeling computations. *Int. J. Numer. Methods Eng.* **2011**, 87, 593–616. DOI:10.1002/nme.3126.
- [63] Eason, E. V.; Hawkes, E. W.; Windheim, M.; Christensen, D. L.; Libby, T.; Cutkosky, M. R. Stress distribution and contact area measurements of a gecko toe using a high-resolution tactile sensor. *Bioinsp. Biomim.* **2015**, 10, 016013. DOI:10.1088/1748-3190/10/1/016013.

- [64] Persson, B. N. J.; Gorb, S. The effect of surface roughness on the adhesion of elastic plates with application to biological systems. *J. Chem. Phys.* **2003**, 119, 11437–11444. DOI:10.1063/1.1621854.
- [65] Rizzo, N. W.; Gardner, K. H.; Walls, D. J.; Keiper-Hrynko, N. M.; Ganzke, T. S.; Hallahan, D. L. Characterization of the structure and composition of gecko adhesive setae. *J. R. Soc. Interface.* **2006**, 3, 441–451. DOI:10.1098/rsif.2005.0097.
- [66] Autumn, K.; Hsieh, S. T.; Dudek, D. M.; Chen, J.; Chitapahan, C.; Full, R. J. Dynamics of geckos running vertically. *J. Exp. Biol.* **2006**, 209, 260–272. DOI:10.1242/jeb.01980.
- [67] Sun, W.; Neuzil, P.; Kustandi, T. S.; Oh, S.; Samper, V.D. The Nature of the Gecko Lizard Adhesive Force. *Biophys. J.* **2005**, 89, L14 – L17. DOI:10.1529/biophysj.105.065268.
- [68] Puthoff, J. B.; Prowse, M. S.; Wilkinson, M.; Autumn, K. Changes in materials properties explain the effects of humidity on gecko adhesion. *J. Exp. Biol.* **2010**, 213, 3699–3704. DOI:10.1242/jeb.047654.
- [69] Prowse, M. S.; Wilkinson, M.; Puthoff, J. B.; Mayer, G.; Autumn, K. Effects of humidity on the mechanical properties of gecko setae. *Acta Biomater.* **2011**, 7, 733–738. DOI:10.1016/j.actbio.2010.09.036.
- [70] Stark, A. Y.; Sullivan, T. W.; Niewiarowski, P. H. The effect of surface water and wetting on gecko adhesion. *J. Exp. Biol.* **2012**, 215, 3080–3086. DOI:10.1242/jeb.070912 .